Nyainqentanglha Shan: A window into the tectonic, thermal, and geochemical evolution of the Lhasa block, southern Tibet

Jessica L. D'Andrea Kapp,[1] T. Mark Harrison,[1,2] Paul Kapp,[3] Marty Grove,[1] Oscar M. Lovera,[1] and Ding Lin[4]

Received 19 July 2004; revised 28 December 2004; accepted 16 March 2005; published 31 August 2005.

[1] In the Nyainqentanglha (NQTL) massif, southern Tibet, a late Cenozoic, SE dipping, normal fault exhumed an oblique section of crust in its footwall. U-Th-Pb dating of zircon and monazite from footwall exposures reveals a collage of felsic intrusions including Cretaceous–early Tertiary and Miocene granitoids. Ages of the latter span >10 m.y., suggesting semicontinuous or episodic Miocene magmatism. Geochemical and isotopic analyses show a Gangdese arc affinity, indicating significant mantle heat and mass transfer in their formation and semicontinuous calc-alkaline magmatism throughout the Cenozoic Indo-Asian collision. The undeformed nature of the footwall Cretaceous and Miocene granitoids suggests that Mesozoic-Cenozoic Lhasa block deformation was "thin-skinned," being concentrated in supracrustal assemblages. This, coupled with the lack of migmatites exposed in the NQTL, implies the exposed crust was not a partial melt zone nor involved in large-scale channel flow. Some $^{40}Ar/^{39}Ar$ thermochronologic studies of footwall K-feldspars reveal that samples collected within several kilometers below the normal fault cooled prior to emplacement of young leucogranites, indicating little perturbation of the background thermal structure since ~15 Ma. This plus high melting temperatures and the lack of penetrative granitoid deformation requires that the melts formed at lower crustal levels and were emplaced rapidly to the midcrust. Seismic reflection results showing high "bright spot" anomalies in the midcrust along the NQTL rift may have imaged the youngest magmatic episode or its associated hydrothermal system.

Citation: Kapp, J. L. D., T. M. Harrison, P. Kapp, M. Grove, O. M. Lovera, and D. Lin (2005), Nyainqentanglha Shan: A window into the tectonic, thermal, and geochemical evolution of the Lhasa block, southern Tibet, *J. Geophys. Res.*, *110*, B08413, doi:10.1029/2004JB003330.

1. Introduction

[2] The exceptional scale and exposure of the active Himalayan-Tibetan orogen (Figure 1) make it a unique natural laboratory for examining the response of the lithosphere to continental collision [*Tapponnier et al.*, 1986, 2001; *Dewey et al.*, 1988; *Harrison et al.*, 1992; *Hodges*, 2000; *Yin and Harrison*, 2000]. Early geologic investigations of this orogen [e.g., *Chang and Zheng*, 1973; *Tapponnier et al.*, 1981; *Allègre et al.*, 1984; *Dewey et al.*, 1988] inspired contrasting interpretations that in part reflected differing views of the strength of the crust-mantle lithosphere system. Advocates of strong lithosphere models believe that a significant proportion of the strain resulting from the Indo-Asian collision has been accommodated on large-scale, strike-slip and thrust faults [e.g., *Argand*, 1924; *Tapponnier et al.*, 1986; *Willett and Beaumont*, 1994; *Owens and Zandt*, 1997; *Meyer et al.*, 1998; *Tapponnier et al.*, 2001; *Wang et al.*, 2001] or by underthrusting of Tibet [e.g., *Powell and Conaghan*, 1973; *Coward et al.*, 1988; *Johnson*, 2002; *DeCelles et al.*, 2002]. Alternatively, weak lithosphere models assume that the crust within the collision zone is fundamentally pliant, possibly due to a partially molten middle crust, and attribute the uplift or collapse of the plateau to a fluid-like behavior [*Dewey and Burke*, 1973; *Zhao and Morgan*, 1985, 1987; *England and Houseman*, 1988; *Bird*, 1991; *Royden*, 1993, 1996; *Nelson et al.*, 1996; *Royden et al.*, 1997; *Huerta et al.*, 1998; *Clark and Royden*, 2000; *Beaumont et al.*, 2001; *Hodges et al.*, 2001]. On the basis of the assumption that the midcrust of Tibet is extensively partial molten, several studies have gone so far as to link midcrustal flow beneath Tibet to south directed extrusion of high-grade rocks along faults bounding the Greater Himalaya Sequence rocks [*Nelson et al.*, 1996; *Beaumont et al.*, 2001, 2004; *Hodges et al.*, 2001; *Grujic et al.*, 2002].

[3] Inferences regarding the physical condition of the middle to deep crust underlying the Tibetan plateau have

[1]Department of Earth and Space Sciences and Institute of Geophysics and Planetary Physics, University of California, Los Angeles, California, USA.
[2]Also at Research School of Earth Sciences, Australian National University, Canberra, ACT, Australia.
[3]Department of Geosciences, University of Arizona, Tucson, Arizona, USA.
[4]Institute of Tibetan Plateau Research, Chinese Academy of Sciences, Beijing, China.

0148-0227/05/2004JB003330$09.00

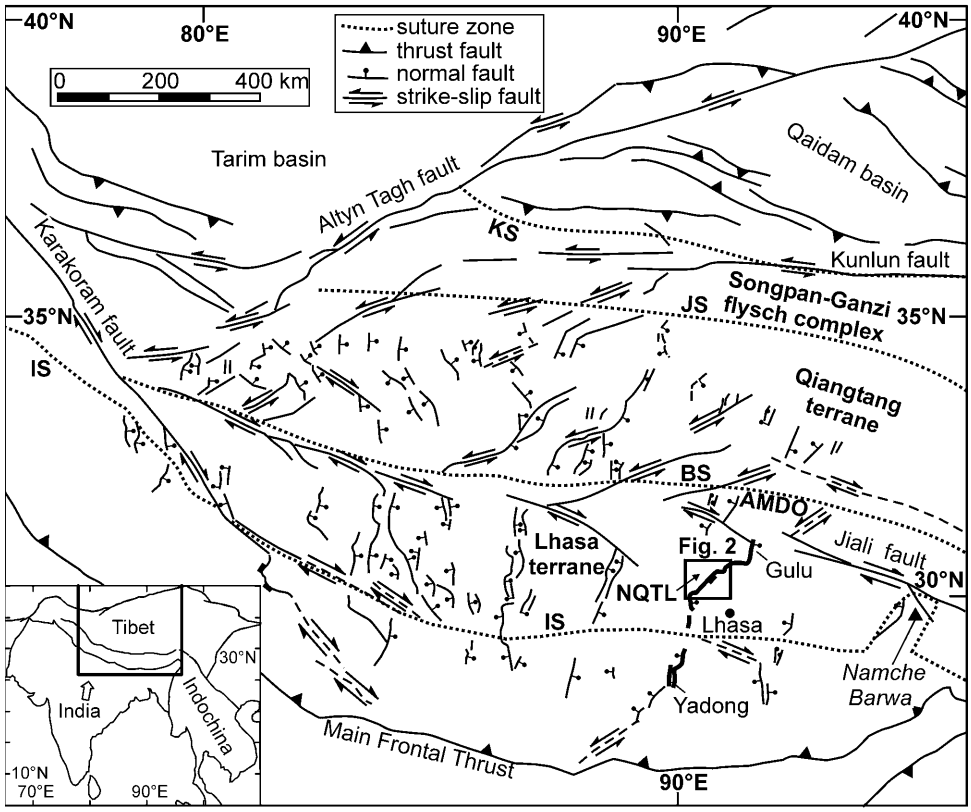

Figure 1. Location map (boxed area in inset). The Nyainqentanglha range (NQTL) of the Lhasa terrane is located along the central segment of the Yadong-Gulu rift (thick-lined faults). Sutures are as follows: BS, Bangong-Nujiang; IS, Indus-Yarlung; JS, Jinsha; and KS, Kunlun. Modified from *Kapp and Guynn* [2004].

been made primarily on the basis of seismic [e.g., *Nelson et al.*, 1996; *Owens and Zandt*, 1997; *Fan and Lay*, 2002; *Vergne et al.*, 2002; *Haines et al.*, 2003; *Xie et al.*, 2004], magnetotelluric [e.g., *Wei et al.*, 2001; *Unsworth et al.*, 2004], and crustal xenolith studies [*Hacker et al.*, 2000; *Ducea et al.*, 2003; *Jolivet et al.*, 2003; *Hacker et al.*, 2005]. Exposures of recently exhumed midcrustal rocks in Tibet that might afford independent insights to evaluate the above models are extremely limited. The Nyainqentanglha (NQTL) massif, located in the central segment of the north trending Yadong-Gulu rift (Figure 1), is the only known locality where midcrustal rocks have been exhumed to the surface in Late Cenozoic time [*Harrison et al.*, 1995]. As such, the NQTL massif presents our only opportunity to gain direct insight into the magmatic and deformation history of southern Tibetan crust.

2. Geological Setting of Southern Tibet

[4] The Lhasa block accreted to southern Asia during Late Jurassic–Early Cretaceous time [*Chang and Zheng*, 1973; *Allègre et al.*, 1984] (Figure 1). It is bounded by the Bangong-Nujiang suture zone to the north, and the Indus-Yarlung suture zone to the south [*Chang and Zheng*, 1973; *Allègre et al.*, 1984; *Dewey et al.*, 1988] (Figure 1). The Lhasa block consists of crust that is presently 60–80 km thick [*Zhao et al.*, 2001; *Kind et al.*, 2002], and supports an average elevation of ~5 km [*Fielding et al.*, 1994]. In addition to the NQTL massif, the only other documented exposure of Tibetan crystalline basement in southern Tibet is Cambrian orthogneiss found near the town of Amdo [*Xu et al.*, 1985] and (Figure 1).

[5] The Lhasa block is pervasively intruded by the Cretaceous-Tertiary Gangdese (Transhimalaya) plutonic belt and is overlain by volcanic rocks of equivalent age [e.g., *Schärer et al.*, 1984; *Xu et al.*, 1985; *Coulon et al.*, 1986; *Debon et al.*, 1986; *Harris et al.*, 1988a; *Quidelleur et al.*, 1997; *Miller et al.*, 1999, 2000; *Harrison et al.*, 2000; *Williams et al.*, 2001; *Chung et al.*, 2003]. Cenozoic contractional deformation is recorded in the development of the Oligocene Gangdese Thrust, which juxtaposed the Gangdese belt southward over Indus-Tsangpo suture mélange and Tethyan sedimentary rocks [*Yin et al.*, 1994, 1999b; *Harrison et al.*, 2000; cf. *Aitchison et al.*, 2003]. The successive development of the Renbu-Zedong Thrust, the Main Central Thrust, and the Main Boundary Thrust reveals a general southward initiation propagation of contractional deformation across the Indus-Tsangpo suture in the Early Miocene to Pliocene [*Hubbard and Harrison*, 1989; *Harrison et al.*, 1997; *Hodges*, 2000; *DeCelles et al.*, 2001, 2002; *Catlos et al.*, 2002] whereas Cenozoic deformation within the Lhasa block was minimal [*Yin et al.*, 1994, 1999b; *Murphy et al.*, 1997].

[6] Despite ongoing convergence between India and southern Asia, the Tibetan plateau is currently undergoing approximately E-W extension by slip along generally north trending rifts and kinematically linked strike-slip faults (Figure 1) [*Molnar and Tapponnier*, 1978; *Armijo et al.*,

1986; *England and Houseman*, 1989; *Yin et al.*, 1999a; *Yin*, 2000; *Blisniuk et al.*, 2001; *Taylor et al.*, 2003]. Tibetan extension has been variably attributed to expansion of the Himalayan arc [*Molnar and Lyon-Caen*, 1989; *Ratschbacher et al.*, 1992, 1994], strain partitioning due to oblique convergence between India and southern Asia [*Seeber and Armbruster*, 1984; *Armijo et al.*, 1986; *McCaffrey and Nabelek*, 1998], convective removal of mantle lithosphere and associated plateau uplift [e.g., *England and Houseman*, 1989; *Molnar et al.*, 1993], gravitational collapse due to maximum sustainable elevation [e.g., *Molnar and Tapponnier*, 1978; *Armijo et al.*, 1986], and rollback of the Pacific margin [*Yin*, 2000]. Whereas Tibetan rifts are generally north trending, their orientations fan systematically from a northwesterly to northeasterly direction from west to east [*Kapp and Guynn*, 2004]. This pattern of rifting is mostly simply explained by collisional stresses along the Himalayan arc and highlights the importance of ongoing collision in influencing the present-day state of stress in the Tibetan upper crust [*Kapp and Guynn*, 2004]. Under the assumption that widespread rifting in southern Tibet is the result of a single phenomenon, the age of rift initiation holds great significance, as it marks a transition in stress regime in southern Tibet from compression to extension. Attempts to constrain the timing of rift initiation in Tibet have generally utilized dating of 18–14 Ma, north trending dikes or fractures, thought to be the expression of extension [*Yin et al.*, 1994; *Coleman and Hodges*, 1995; *Williams et al.*, 2001]. However, previous thermochronological study of the NQTL massif [*Harrison et al.*, 1992, 1995; *Stockli et al.*, 2002] have indicated later extension with normal faulting initiating at circa 8 ± 1 Ma for the Yangbajain portion of the rift, and ~5 Ma for the Gulu portion of the rift (Figure 1).

[7] Geologic mapping of southeast Tibet [*Kidd et al.*, 1988; *Liu*, 1988; *Wu et al.*, 2004] reveals the existence of an extensive supracrustal sequence that includes (1) undifferentiated Paleozoic limestone, sandstone and shale, (2) Carboniferous-Permian mudstone, siltstone, and sandstone, (3) Permian limestone and shale, (4) Jurassic–Lower Cretaceous sandstone, shale and flysch, (5) Aptian-Albian limestone and Upper Cretaceous red beds of the Takena Formation, and (6) Paleocene-Eocene (60–49 Ma) volcanic sequences of the Linzizong Formation [see *Kidd et al.*, 1988]. Of particular note is the fact that the Upper Cretaceous Takena Formation is highly shortened but unconformably overlain by the flat-lying or gently folded Linzizong volcanic sequence [*Burg et al.*, 1983; *Allègre et al.*, 1984; *Burg and Chen*, 1984; *Pan*, 1993]. This relationship is ubiquitous throughout the Lhasa block [*Liu*, 1988; *Murphy et al.*, 1997].

3. Geology of the Nyainqentanglha Massif

[8] Our understanding of the geology of the NQTL massif is based on previous field studies and our lithologic and structural mapping on 1:100,000 scale topographic maps. Previous efforts established the first-order geologic framework of the most easily accessible margins of the NQTL. In this study, we extended detailed observation by systematically mapping and sampling the massif along traverses into the deeply incised valleys. Our results complement and allow refinement of previous structural interpretations [*Pan and Kidd*, 1992; *Harrison et al.*, 1995; *Cogan et al.*, 1998] and unambiguously document the contact relations between undeformed granites and strongly deformed orthogneisses and metasedimentary rocks in the NQTL massif.

3.1. Rock Units

[9] The NQTL massif largely exposes Cretaceous-Tertiary granitoids and orthogneisses [*Kidd et al.*, 1988] and metasedimentary lithologies that range in age from Paleozoic [*Kidd et al.*, 1988] to Cretaceous [*Edwards and Ratschbacher*, 2005] (Foldout 1). The metasedimentary lithologies on the northwest side of the NQTL massif consist of slate, phyllite, metaconglomerate and metalimestone, whereas those exposed along the road from Damxung to Nam Co (Foldout 1) also include biotite-garnet schists and staurolite-bearing schist [*Coward et al.*, 1988; *Harris et al.*, 1988b; *Pan and Kidd*, 1992; *Pan*, 1993; *Harrison et al.*, 1995; *Edwards and Ratschbacher*, 2005]. Pelitic metasedimentary rocks locally contain andalusite indicating low-pressure contact metamorphism during emplacement of granites [*Coward et al.*, 1988].

[10] To the east of the NQTL massif are Carboniferous shallow marine clastic deposits and minor limestone (Foldout 1). The northwesternmost flank of the NQTL range exposes red sandstone, mudstone, and conglomerate of previously inferred Late Cretaceous age [*Kidd et al.*, 1988; *Liu*, 1988]. This age assignment is confirmed by our observations that Aptian-Albian limestone clasts-bearing red beds are intruded in several places by earliest Tertiary granites (Foldout 1). Paleocene-Eocene volcanic sequences of the Linzizong Formation are widespread to the south of the NQTL massif [*Coulon et al.*, 1986; *Kidd et al.*, 1988] (Foldout 1). Volcanic rocks of Neogene age (Maqiang Formation; 10–14 Ma) are less voluminous and restricted to the area southwest, and along strike, of the NQTL massif outside of the area shown in Foldout 1 [*Coulon et al.*, 1986; *Kidd et al.*, 1988]. Within the NE trending, 5 to 15 km wide graben between Yangbajain and Damxung (Foldout 1) are Quaternary glacial, alluvial fan, fluvial, and lacustrine deposits. The graben fill over much of the rift is generally less than a few hundred meters in thickness, with a maximum thickness of ~1500 m, and thickens to the southeast away from the NQTL massif [*Cogan*, 1995; *Alsdorf et al.*, 1998; *Cogan et al.*, 1998].

3.2. NQTL Detachment Fault and Shear Zone

[11] The low-angle fault defining the range front of the NQTL was initially interpreted to be a low-angle thrust fault [*Allègre et al.*, 1984]. However, the (1) top to the southeast sense of shear in footwall mylonites, (2) presence of mesoscopic normal faults in fault zone chloritic breccia, (3) similarities in the orientation and kinematics of the shear zone, low-angle fault, and most prominent high-angle normal faults within the Yangbajain-Damxung graben, and (4) juxtaposition of strongly tectonized rocks in the footwall against graben fill in the hanging wall clearly indicate that it is a low-angle normal (detachment) fault. The southeast dipping, low-angle (22°–37°) fault surface is locally exposed along the southeastern range front of the NQTL massif (in red and labeled as Nyainqentanglha detachment in Foldout 1). Fault surface striations generally trend down-

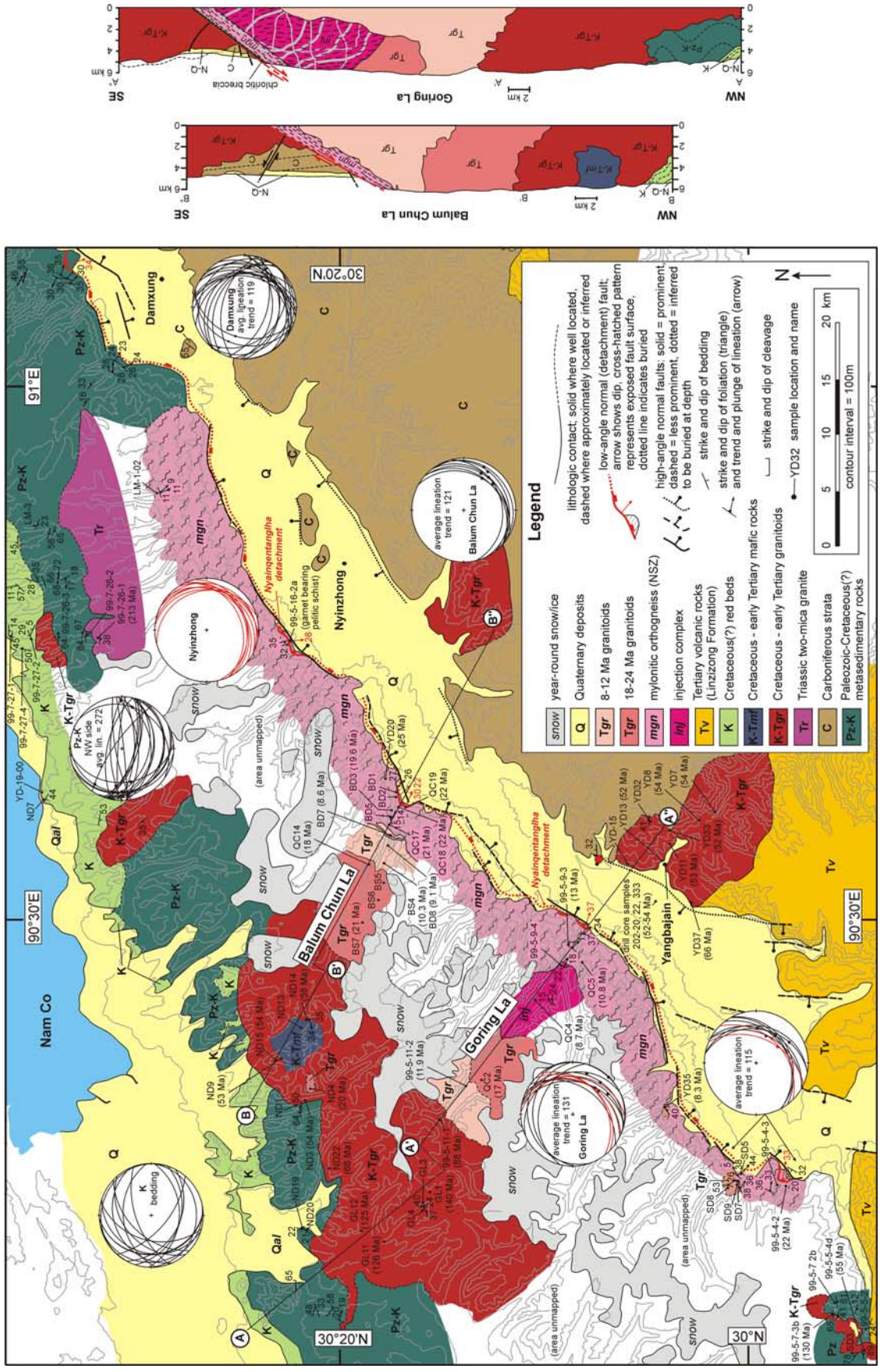

Foldout 1. Geologic map and cross sections of the Nyainqentanglha massif. Lower hemisphere, equal-area stereonets show orientations of foliation (black great circles), stretching lineations (black dots), mesoscopic brittle normal faults (red great circles) and slickenlines (red dots) in chloritic breccia.

dip to the southeast [*Pan and Kidd*, 1992; *Harrison et al.*, 1995]. The low-angle fault surface is in many places unconformably overlain by Quaternary alluvial fan and fluvial conglomerates. However, northwest dipping Neogene-Quaternary(?) conglomerates occur in the hanging wall of the southernmost fault exposure mapped, indicating that the fault was active during latest Cenozoic time (Foldout 1).

[12] The low-angle fault is structurally underlain by a 1- to 2-km-thick shear zone in its footwall, consisting of metasedimentary rocks north of Damxung and orthogneisses everywhere to the south (Foldout 1). The shear zone exhibits a well developed foliation that is variable, but generally dips gently (<35°) to the southeast, and a stretching lineation (defined in most places by quartz) that trends 115°–131° (S65°E to S49°E) (see stereonets accompanying Foldout 1). The orthogneisses consist of plagioclase, K-feldspar, quartz, minor biotite and/or muscovite aligned in the direction of the stretching lineation, and locally garnet. It becomes progressively coarser-grained with structural distance below the range front low-angle fault. South of Nyinzhong, the shear zone is intruded by mildly deformed to undeformed granitoids at a distance of 1 to 5 km into the range away from the low-angle fault.

[13] In some places, the range front low-angle fault is separated from underlying orthogneisses by a 10- to 20-m-thick zone of chloritic breccia. Within the breccia are mesoscopic gently to moderately dipping (12°–50°) brittle faults with normal separation that are synthetic to the main low-angle fault (see stereonets accompanying Foldout 1). S-C fabrics in footwall mylonitic orthogneisses consistently indicate a top to the southeast sense of shear [*Pan and Kidd*, 1992; *Pan*, 1993]. We confirmed this result along all transects through the shear zone.

[14] To the southeast of the range front low-angle fault are high-angle (≥60°) faults that cut fill of the Yanbajain-Damxung graben. The magnitude of slip along these faults ranges from meters to hundreds of meters [*Armijo et al.*, 1986; *Coward et al.*, 1988; *Pan and Kidd*, 1992] (Foldout 1). The strikes of the high-angle faults closely mimic the orientation of the graben-bounding ranges. Those with northeasterly strikes exhibit dominantly dip-slip normal displacement whereas those with a more easterly strike exhibit a significant component of left-lateral separation [*Armijo et al.*, 1986]. The Neogene to active faulting of the Yangbajain-Damxung graben is accompanied by active hydrothermal systems [*Armijo et al.*, 1986; *Yokoyama et al.*, 1999; *Hoke et al.*, 2000]. The high-angle faults that have produced the most prominent fault scarps are located along the northwest side of the graben [*Armijo et al.*, 1986], and in places, within tens of meters to the southeast of the range front low-angle fault (Foldout 1). However, no high-angle faults of significant displacement (greater than tens of meters) were observed to cut shear zone rocks in the footwall of the range front low-angle fault.

[15] Since the work of *Pan and Kidd* [1992], the NQTL detachment fault and underlying shear zone have been accepted to be manifestations of the late Cenozoic extensional tectonic regime of southern Tibet [e.g., *Harrison et al.*, 1995; *Cogan et al.*, 1998]. These structural features may extend largely undisrupted to the southeast beneath the graben as indicated by the presence of a low-angle (~30°), easterly dipping seismic reflector beneath the Nyinzhong area (Foldout 1) which projects updip toward the surface trace of the NQTL detachment [*Cogan et al.*, 1998]. The NQTL detachment fault and shear zone terminate along strike to the southwest where the trend of the NQTL massif changes from a northeasterly to northerly direction and exhibits a decrease in overall relief (Foldout 1). Here extensional deformation is characterized by a 15-km-wide zone of distributed high-angle normal faults that cut Linzizong volcanic rocks (Foldout 1) [*Armijo et al.*, 1986; *Kidd et al.*, 1988]. To the northeast of the area shown in Foldout 1 the NQTL massif exhibits a change from a northeasterly to easterly trend (Figure 1). In this area, Paleozoic-Cretaceous metasedimentary rocks of the NQTL massif are deformed by an east-west striking transtensional shear zone that is suggested to have been active during Late Cenozoic time [*Edwards and Ratschbacher*, 2005]. Additional studies are needed to clarify the timing and kinematic relationships between this transtensional shear zone and the NQTL to the south.

3.3. Geology of the Hanging Wall

[16] Within the Yangbajain-Damxung graben, hanging wall lithologies are exposed sporadically in hills within the rift basin that are not mantled by the thin sedimentary sequence that infills the graben elsewhere [*Cogan et al.*, 1998] (Foldout 1). They are composed of early Tertiary Linzizong volcanic rocks or Carboniferous sedimentary rocks. The hanging wall strata generally dip toward the range front [*Kidd et al.*, 1988; *Pan and Kidd*, 1992; this study]. This relationship implies a listric geometry for the southeast dipping normal faults along the southeastern flank of the NQTL massif. East of the graben, Carboniferous strata generally dip northward and strike obliquely to the graben [*Pan and Kidd*, 1992; this study]. The northward dip is attributed to preextensional contractional deformation and is accompanied by upright to south verging folds [*Coward et al.*, 1988]. The Carboniferous strata are intruded by undeformed, latest Cretaceous–earliest Tertiary granitoids of the Gangdese batholith [*Xu et al.*, 1985] (also this study; see section 4) and unconformably overlain by gently dipping Linzizong volcanic rocks [*Coulon et al.*, 1986; *Kidd et al.*, 1988; *Liu*, 1988]. We interpret the angular unconformity to indicate that Carboniferous strata in the NQTL area were shortened and locally exhumed to the surface prior to the Indo-Asian collision.

3.4. Geology of the Footwall

[17] The footwall of the NQTL shear zone consists predominantly of an assemblage of undeformed Cretaceous–early Tertiary plutons and lower to middle amphibolite facies wall rocks that were later intruded by Miocene granitoids (Foldout 1). Although we investigated many of the valleys transecting the NQTL massif, the Balum Chun La and Goring La transects (Foldout 1) provide the best exposed and most complete picture of the cross sectional relationships of the footwall (Foldout 1). In the Balum Chun La valley (Foldout 1), kilometer-scale Miocene biotite granites of various ages exhibit intrusive contact relationships. The northwest part of the valley consists entirely of Cretaceous–early Tertiary granitoids, and minor diorite and mafic cumulates (Foldout 1).

[18] In the Goring La valley (Foldout 1), ~5 km structurally below the NQTL detachment fault, there is an "injection complex" where foliated but weakly lineated orthogneiss is intruded by meter-scale-thick leucogranite sills and dikes. The dikes can be divided into two sets based on their orientations: subvertical dikes (at least some of which are Miocene; see section 4) and cross-cutting dikes which exhibit northeastward and northwestward dips of ~60° (Figure 2). We interpret the subvertical dikes to have intruded along tensile fractures that form parallel to the greatest principal stress direction (σ_1). We interpret the cross-cutting dikes to have intruded along conjugate normal-sense shear fractures, that form at ~30° to σ_1 [*Davis and Reynolds*, 1996]. Given that the present-day state of stress in the southern Tibetan upper crust is characterized by a vertical σ_1 [e.g., *Mercier et al.*, 1987; *Ratschbacher et al.*, 1994], the above interpretations suggest that the present-day orientation of the dikes is probably similar to their original orientation at the time of emplacement. Approximately 13 km up the valley from the NQTL detachment fault, the injection complex is intruded by a kilometer-scale body of undeformed biotite granite (Foldout 1). Further to the northwest, this body is itself intruded by a younger biotite granite (Foldout 1).

[19] Along the northwestern flank of the NQTL massif, Upper Cretaceous red beds unconformably overlie Paleozoic-Cretaceous metasedimentary rocks (Foldout 1). The red beds are deformed by east-west trending upright folds of variable wavelength (tens of meters to kilometers). The metasedimentary rocks are locally foliated and lineated, with stretching lineations trending distinctly more east-west than those of the NQTL shear zone (see stereonets accompanying Foldout 1). The regional relationship between the trace of the unconformity beneath the red beds and topography suggests that the unconformity generally dips moderately (30° to 50°) to the northwest in the area of Foldout 1. The northwest dip of the unconformity increases along strike to the northeast where it is subvertical to overturned at Lagen La pass north of Damxung [*Edwards and Ratschbacher*, 2005; this study]. Both the metasedimentary rocks and overlying Upper Cretaceous red beds are intruded by undeformed Cretaceous–early Tertiary granites.

4. Geochronological Studies of Zircon and Monazite

[20] The extensive exposure of foliated crystalline rocks in the NQTL massif led *Liu* [1988] to speculate that the core of the NQTL range was primarily Precambrian basement rocks. However, conventional U-Pb analyses of zircons from NQTL shear zone gneisses yielded ages of ~50 Ma, with a hint of a late Tertiary component [*Xu et al.*, 1985]. More recently, two undeformed Miocene (18 Ma and 11 Ma) granite bodies from the massif were documented by *Liu et al.* [2004]. In this study, ion microprobe spot analysis and depth profiling studies clearly demonstrate that the NQTL crystalline complex is composed of a number of granitoid bodies ranging in age from Triassic (~210 Ma) to Late Miocene (~8 Ma).

4.1. Methods and Sample Preparation

[21] Zircon and monazite grains were separated from fresh granitoid and gneiss samples using standard separation techniques and analyzed for U-Th-Pb age using the methods described by *Quidelleur et al.* [1997] and *Schmitt et al.* [2003] for spot analyses and *Grove and Harrison* [1999] for depth profiling. Zircon ages were determined relative to AS-3, a concordant zircon standard with an age of 1099.1 ± 0.5 Ma [*Paces and Miller*, 1993; *Schmitz et al.*, 2003] and Th-Pb monazite ages relative to the 45.3 ± 1.4 Ma standard 554 [*Harrison et al.*, 1999]. In spot analysis mode, the primary beam was focused on selected sites within the grain, and usually either the centers of grains (possible cores) or near the rims (possibly the youngest growth zones) were targeted. Backscattered electron (BSE), cathodoluminescence (CL), and/or optical images were used to select targets within grains or were obtained after analyses to determine whether multiple zones were analyzed either within one spot or in different spots (see section 4.4). Typical ~15-min spot analyses used a spatial resolution of 10–20 μm and produced a crater depth of ~2 μm.

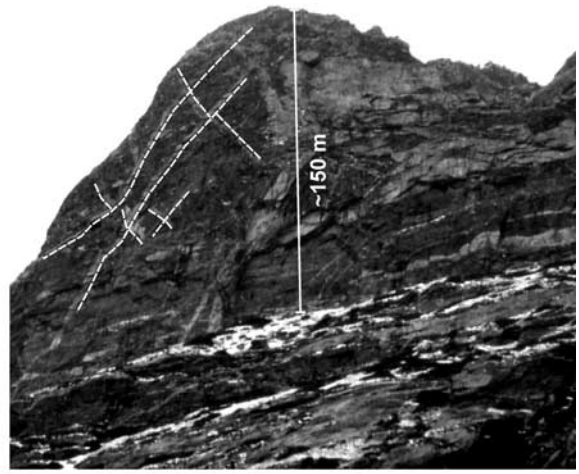

Figure 2. Miocene injection complex of the Goring La valley showing cross-cutting dikes (highlighted by white dashed lines) that are interpreted to have been emplaced along conjugate normal-sense shear fractures. View is toward the north.

[22] For depth profiles, two approaches were used. The first was to sputter a crater into an unpolished crystal for up to 90 min producing pits of 5–8 μm. This approach often resulted in unstable U-Pb calibrations as a result of sample charging. Alternatively, the serial sectioning technique of *Mojzsis and Harrison* [2002] was employed in which the crater depth from the initial sputtering was measured using a surface profilimeter and then the sample was further polished and analyzed. By repeating the process several times, 5–8 μm craters with stable interelement calibrations and uniform pit profiles were routinely achieved.

4.2. Results of Zircon and Monazite Spot Analyses

[23] Interpreted age results from all spot analyses for zircon and monazite, organized by sample name, are summarized in Table 1. A complete compilation is provided in the auxiliary material[1] (Table A1 for zircon results and Table A2 for monazite results). The main conclusions drawn

[1] Auxiliary material is available at ftp://ftp.agu.org/apend/jb/2004JB003330.

Table 1. Interpreted Ages of Rock Crystallization and Inheritance Based on U-(Th)-Pb Ion Microprobe Spot Analyses on Single Monazite and Zircon Grains

Sample	Age, Ma	2σ	Number of Grains	Interpretation
QC4	8.7	0.3	13	crystallization
YD-35	8.3	0.3	3	crystallization
YD-35	9.2	0.3	3	inheritance
BD-8	9.1	0.4	16	crystallization
BS-4	10.3	0.3	4	crystallization
QC5	10.8	0.3	5	crystallization
QC5	15.5	0.4	4	inheritance
BD-7	8.6	0.2	2	crystallization
BD-7	10.0	0.2	3	inheritance
BD-7	12.8	0.4	2	inheritance
99-5-11-2	11.9	0.3	9	crystallization
99-5-11-2	16.0	0.4	4	inheritance
99-5-9-3	13.0	0.4	11	crystallization
QC14	18.2	0.5	14	crystallization
QC14	50.9	1.2	3	inheritance
QC14	63.2	1.5	1	inheritance
QC14	69.4	2.3	1	inheritance
QC14	154.5	5.7	1	inheritance
BD-3	19.6	0.4	2	crystallization
BD-3	21.8	0.5	6	inheritance
QC2	16.8	0.5	3	crystallization
QC2	22.2	0.6	16	inheritance
QC2	64.5	2.2	2	inheritance
QC2	194.7	7.3	1	inheritance
QC17	20.6	0.5	6	crystallization
QC17	37.1	1.6	1	inheritance
QC17	49.9	1.5	2	inheritance
QC17	104.7	4.8	1	inheritance
QC17	128.8	4.6	1	inheritance
QC18	21.9	0.5	13	crystallization
QC18	79.1	2.2	1	inheritance
QC18	131.0	3.5	1	inheritance
QC18	193.2	7.6	1	inheritance
QC19	22.1	0.5	11	crystallization
QC19	54.6	1.6	3	inheritance
99-5-4-2	21.7	1.0	1	crystallization
99-5-4-2	32.4	1.1	4	inheritance
BS-7	21.0	0.5	6	crystallization
BS-7	50.8	3.3	1	inheritance
BS-7	89.6	4.6	1	inheritance
ND-4	20.0	0.5	5	crystallization
ND-4	24.2	0.5	6	inheritance
YD-20	24.8	1.6	2	crystallization
YD-33	52.0	1.3	9	crystallization
202-22	53.9	2.0	9	crystallization
202-33	51.8	2.6	7	crystallization
202-20	52.8	1.6	8	crystallization
202-20	124.5	6.7	1	inheritance
ND-9	53.3	1.2	16	crystallization
ND-9	59.2	3.1	3	inheritance
ND-9	66.7	1.7	1	inheritance
YD-13	52.5	1.3	9	crystallization
YD-13	57.0	1.5	3	inheritance
YD-11	53.3	1.6	7	crystallization
YD-11	56.9	1.9	1	inheritance
ND-15	53.5	1.3	5	crystallization
ND-15	56.4	2.1	1	inheritance
ND-15	61.0	2.2	1	inheritance
99-5-2-1a	53.9	1.7	3	crystallization
99-5-2-1a	60.1	3.7	1	inheritance
99-5-5-4d	54.8	1.7	5	crystallization
99-5-5-4d	65.7	3.7	1	inheritance
99-5-5-4d	70.2	3.8	1	inheritance
YD-7	53.9	1.7	7	crystallization
YD-8	54.1	2.0	7	crystallization
YD-8	62.6	2.7	1	inheritance
YD-8	97.7	4.2	2	inheritance
ND-14	58.4	1.5	6	crystallization
ND-3	35.4	1.7	1	crystallization
ND-3	54.1	2.0	7	inheritance
99-5-9-4a	60.9	3.1	5	crystallization
99-5-9-4a	181.1	5.8	3	inheritance
YD-37	65.6	2.2	8	crystallization
ND-22	66.5	1.7	2	crystallization
99-5-11-1a	87.9	3.0	8	crystallization
GL-12	125.0	3.2	7	crystallization
GL-12	204.0	7.4	1	inheritance
GL-11	126.3	5.0	4	crystallization
GL-11	154.4	10.2	1	inheritance
99-5-7-3b	130.0	4.0	4	crystallization
GL-1	140.5	3.1	3	crystallization
GL-1	145.2	3.3	2	inheritance
GL-1	165.3	8.9	1	inheritance
99-7-26-1b	212.7	5.1	23	crystallization

from these analyses are summarized below. Unless otherwise specified, zircon ages reported in the text refer to $^{206}Pb/^{238}U$ values and monazite ages to $^{208}Pb/^{232}Th$ results.

[24] All samples from the hanging wall of the NQTL detachment yield ages characteristic of Gangdese arc magmatism (50–60 Ma). Three granitoid samples from a drill core (194 m, 222 m, and 336 m depths) near Yangbajain (provided by Zhiguo Mu, Peking University), are ~53 Ma (see Foldout 1 for location).

[25] Zircon U-Pb age results from the footwall granitoids are highly complex. The ages obtained from virtually all samples ranged from Early Cretaceous (~140 Ma) to Late Miocene (~8 Ma). However, one two-mica granite body yielded a ~211 Ma age that we interpret as a potential product of Triassic rifting of the Lhasa block from Gondwana [*Leeder et al.*, 1988; *Pearce and Mei*, 1988].

[26] In the case of the Miocene granitoids, spot analyses of individual zircons varied by as much as 10 m.y. (e.g., Figure 3) or more than 5 times the expected scatter expected for homogeneous materials given the variability of the standard results. A few samples yielded uniform ages of 8–9 Ma. More typically, individual samples showed two distinct age populations. In addition, zircons with Miocene rims overgrowing Cretaceous cores were detected. These restitic materials presumably reflect assimilation of Gangdese age plutons in the source region.

[27] Because of the near linear form of $^{206}Pb/^{238}U$ versus $^{207}Pb/^{235}U$ concordia for Late Mesozoic and Cenozoic time, there is very little that can be meaningfully done to interpret our results in terms of a mixture of igneous crystallization and/or metamorphic recrystallization ages on a concordia plot (see Figure 3b). Given this limitation, we have simply elected to plot the results in terms of the probability density of the $^{206}Pb/^{238}U$ ages. Doing so reveals clear peaks for the entire population of samples at ~10 Ma, ~21 Ma, and ~53 Ma (Figure 4a). The Miocene peaks (Figure 4b) are quite consistent with *Liu et al.*'s [2004] more limited data set. The less distinct Early Cretaceous peak presumably reflects contamination from the Gangdese arc. While the plot is only scaled to 250 Ma, Pan-African (~550 Ma) and older (~2.5 Ga) zircon is also present in trace amounts (~1%).

[28] Interestingly, Th-Pb analysis of monazite produced essentially the same range of ages (21–8 Ma) as did coexisting zircon (Figure 4c). In contrast to the case for zircon, only minor Cretaceous or older inheritance was detected (Figure 4d). The fact that both monazite and zircon

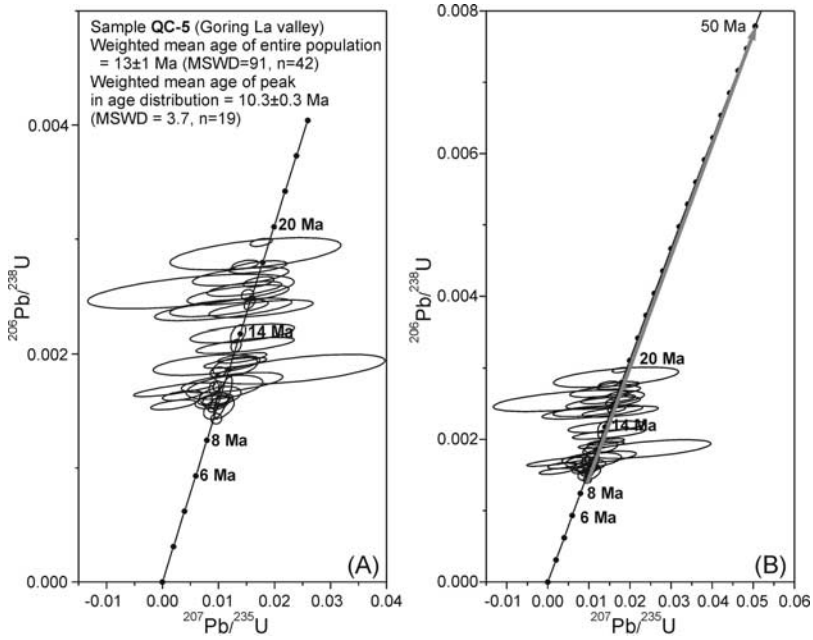

Figure 3. (a) Example of age range seen within a single sample of NQTL leucogranite. (b) Problem with discordia line between Gangdese age (~50 Ma) inheritance and young leucogranites. Ages would cover a range that lies along concordia, making it difficult to distinguish between a single (lower intercept) age and real, distinct formation or metamorphic recrystallization age.

exhibited a similar age range favors essentially simultaneous crystallization of both phases since each are characterized by relatively high Pb closure temperatures [*Cherniak et al.*, 2004]. In a few cases, monazite ages were slightly younger than the coexisting zircon suggesting possible recrystallization effects [*Cherniak et al.*, 2004].

[29] Finally, two samples of orthogneiss from the NSZ were analyzed. Sample 99-5-9-4 (Foldout 1) yielded an age of 59 ± 0.5 Ma. We interpret the results to indicate that the protolith was a Gangdese age granitoid. Sample 99-5-9-3 (Foldout 1) yielded a ~13 Ma age, indicating that late Tertiary granitoids were also involved in the NQTL shear zone deformation. A granitoid clast (sample LM-3, Foldout 1) in footwall metasedimentary rocks from the northwest side of the range, mapped by *Liu* [1988] as Paleozoic, yielded a ~120 Ma age indicating that the sediment protolith is Cretaceous or younger.

4.3. Results of Depth Profiling of Zircon and Monazite

[30] To evaluate the possibility of protracted crystallization histories, ion microprobe depth profiles of both zircon and monazite were performed. The goal was to discern whether age variations occur within single crystals of zircon and/or monazite, and whether the age variations reflect continuous growth or episodic growth/recrystallization.

[31] Depth profiles of unpolished individual zircons commonly revealed appreciable age variations in the outer 1–10 μm. In general, age results from the outer ~1 μm or so of unpolished crystals are between 8 and 10 Ma (see Table A3 in auxiliary material). This is an important observation, because samples that yielded isochronous results in depth profiling mode were mostly the youngest results, between 8 and 10 Ma in age. For example, sample BD-8-00, a granitoid from Balum Chun valley (Foldout 1), consistently yielded ages of 8–9 Ma over the 3.5 μm of depth profiling.

[32] Because crater bottoms are not completely flat, each age in a depth profile may be a mixture between zones of differing age. As a result, age increases with increasing depth into the crystal are interpreted as reflecting mixing between young, very thin overgrowths and older, mostly Gangdese age, cores as opposed to continuous growth over a protracted time. Of note is the correlation between young ages obtained from the outer 1–2 μm of unpolished zircons, and Th/U ratios. Th/U as low as 0.02, increasing with age, are commonly seen for zircon rims. For example, sample QC-19 has an initial age (outer 2 μm) of ~8 Ma and a corresponding Th/U of 0.02 (Figure 5). As age increases to circa 18 Ma, Th/U rises to 0.16 (Figure 5). This behavior most likely reflects mixing between two end-member ages; ~8 Ma, and ~53 Ma (the spot analysis age; see Table 1). This correlation between Th/U and age is typical for NQTL granitoids (see Table A3) and interpreted to reflect overgrowths precipitated from a low Th/U aqueous fluid at circa 8–10 Ma as such low Th/U values are typical of metamorphic fluids [*Mojzsis and Harrison*, 2002]. Assuming that whole rock Th/U is representative of the melt from which the zircon initially crystallized, the ultralow Th/U ratios cannot reflect magmatic growth. For example, in the case of sample 99-5-9-3, the outer 0.8 μm yields an age of ~10 Ma with corresponding Th/U of ~0.04 (Figure 6) which corresponds to a magmatic Th/U of ~0.2 [*Schmitt et al.*, 2003]. This is 30 times lower than the whole rock Th/U of 6 (Table 2). Even in the presence of monazite crystallization it is unlikely that the rims reflect magmatic crystallization.

[33] Age variations seen during extended depth profiling sessions, particularly jumps in age, sometimes correlate to

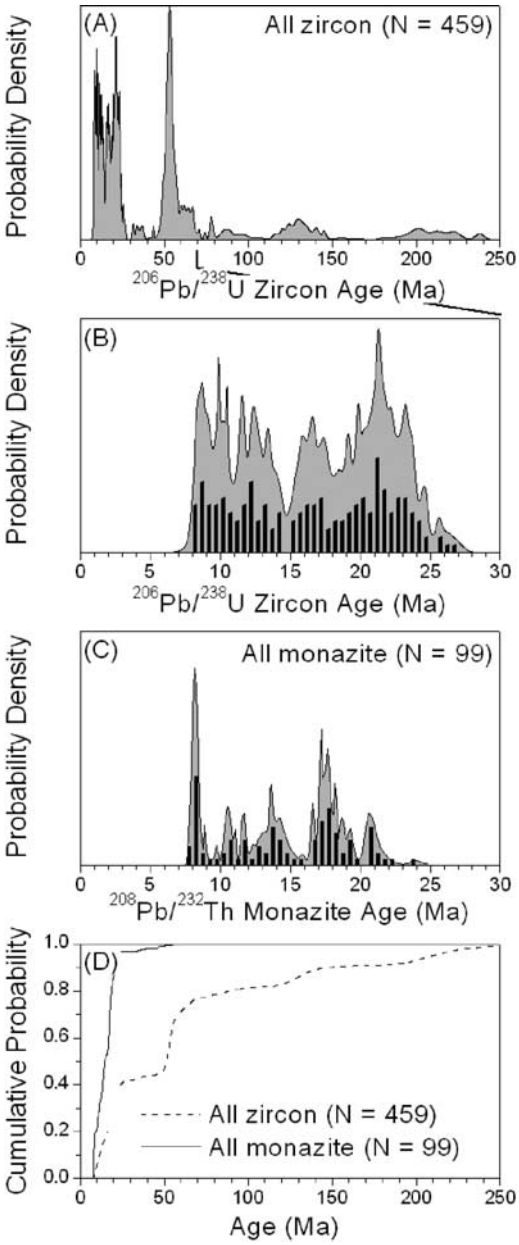

Figure 4. (a) Probability density distribution of all zircon spot analyses from Nyainqentanglha granitoids. Peaks define distinct magmatic episodes at ~10, ~21, and ~53 Ma. Smaller pulses occur at ~130 and ~210 Ma. (b) Expanded scale of zircon analyses with superposed histogram (0–30 Ma). (c) Probability density distribution of all monazite spot analyses with superposed histogram (0–30 Ma). (d) Cumulative probability distributions for all zircon and monazite spot analyses. Note that >95% of monazite are less than 25 Ma, while only 42% of zircon spot analyses are less than 25 Ma.

changes in UO^+/U^+ (i.e., calibration artifacts) and thus should be regarded with caution. While we attempted to minimize this problem by resetting energy offsets every ~10 min (i.e., to offset sample charging effects), such efforts did not eliminate this effect. However, cases where analyses of unpolished surfaces yielded ages as young as 8 Ma and Cretaceous or older after polishing are clearly recording complex, protracted growth histories.

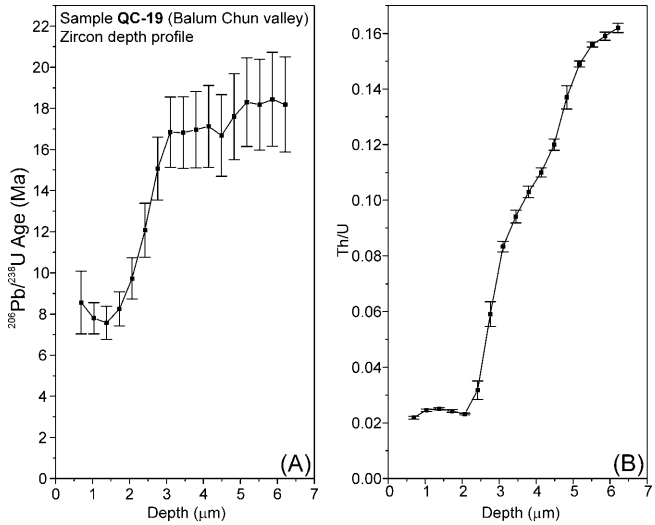

Figure 5. (a) Age versus depth for a zircon for sample QC-19 from Balum Chun La valley. (b) Th/U versus depth for same analysis. The steady change in Th/U corresponds to the steady age increase with depth, suggesting that the age variation is real, with the rim of the zircon revealing metamorphic or hydrothermal overgrowth at ~8 Ma, while the core is ~18 Ma.

[34] Depth profiling of selected monazites revealed no significant age variations (Figure 7). See Table A4 for a compilation of all monazite Th-Pb depth profiling results.

4.4. Image Analysis

[35] To help address the question of whether zircon age variations represent continuous growth over a protracted

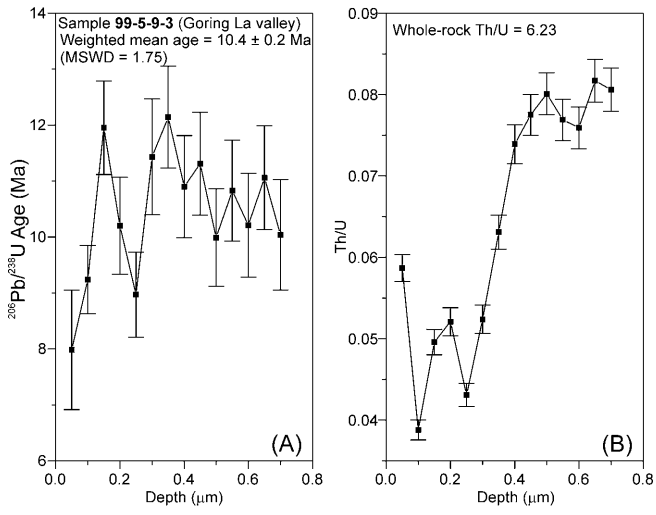

Figure 6. (a) Age versus depth for sample 99-5-9-3 from Goring La valley. (b) Th/U versus depth for same analysis. The whole rock Th/U of this sample is 6.23. The low values of Th/U in the analyzed spot suggest the outer rim of this zircon did not simply precipitate from a magma but instead may have formed by hydrothermal precipitation or metamorphic overgrowth.

Table 2. Major and Trace Element Concentrations of Granitoid Samples From the Nyainqentanglha Crystalline Complex[a]

	QC-2	QC-4	QC-5	QC-14	QC-17	QC-18	QC-19
SiO_2	72.8	76.8	73.0	68.9	74.3	74.4	75.0
Al_2O_3	13.6	12.8	15.0	14.9	14.2	14.2	13.3
C_aO	1.69	0.74	0.38	1.77	1.23	1.36	0.98
MgO	0.3	0.01	0.02	0.46	0.11	0.22	0.07
Na_2O	3.09	3.15	2.58	3.24	3.39	3.79	3.29
K_2O	4.92	4.92	8.19	5.41	5.08	4.5	4.95
Fe_2O_3	1.85	0.68	0.31	2.39	1	1.29	0.85
FeO	1.66	0.61	0.28	2.15	0.90	1.16	0.76
MnO	0.05	0.02	0.05	0.06	0.03	0.038	0.04
TiO_2	0.266	0.065	0.018	0.304	0.109	0.138	0.077
P_2O_5	0.06	0.01	0.04	0.1	0.02	0.03	0.02
LOI	0.35	0.45	0.25	0.45	0.4	0.35	0.6
Sum	99.1	99.8	99.9	98.3	100	100.28	99.2
V	13	2	null	28	8	7	4
Co	130	null	null	3	2	2	2
Ni	6	5	4	6	17	null	2
Cu	1.5	2.3	1.7	5.7	3.5	11	4.7
Zn	45.1	22.5	11	63.5	30.9	37	37.2
Ga	16	14	16	17	15	18	13
Rb	331	335	599	435	392	335	409
Sr	122	37.4	115	290	106	113	56.6
Y	25	21	18	31	44	44.5	60
Zr	221	37	27	279	121	104	89
Nb	31	19	23	48	26	17.3	23
Ba	331	91	361	956	311	330	148
La	134	9.6	10.7	89.6	35.8	30.6	26.6
Ce	275	20.2	22.2	159	69.4	59.8	53.4
Pr	27.1	2.2	2.4	15	6.9	6.18	5.7
Nd	98.5	7.5	9	49.3	25.9	21.8	20.6
Sm	16.2	2.3	2.4	6.3	5.5	4.63	5.3
Eu	1.05	0.25	0.56	1.09	0.43	0.457	0.37
Gd	11.6	2.7	2.2	4.8	5.4	4.21	1.2
Tb	1.2	0.5	0.4	0.6	1	1	1.2
Dy	5.8	3.5	2.9	4.6	6.7	6.7	9.6
Ho	0.86	0.68	0.5	0.93	1.43	1.42	1.91
Er	2.3	2.1	1.7	3.7	4.4	4.69	6.2
Tm	0.3	0.3	0.3	0.6	0.7	0.751	1
Yb	1.6	1.9	2	4.4	4.6	4.91	6.3
Lu	0.2	0.23	0.29	0.6	0.63	0.698	0.85
Th	null	null	null	null	null	39.7	null
Pb	null	null	null	null	null	41	null
U	null	null	null	null	null	21.3	null
	99-5-4-2	99-5-9-3	99-5-11-2	ND-4-00	BD-3-00	BD-7-00	BD-8-00
SiO_2	70.8	74.5	72.7	70.9	74.3	73.1	78.8
Al_2O_3	14.7	13.7	14.5	15.2	13.5	14.3	12.0
C_aO	1.72	1.3	1.16	1.62	0.72	1.36	0.49
MgO	0.55	0.34	0.22	0.51	0.22	0.35	0.03
Na_2O	3.55	3.04	3.37	3.29	3.59	3.59	2.62
K_2O	5.36	5.27	6.03	5.66	5.33	4.65	5.31
Fe_2O_3	2.78	1.61	1.67	2.23	1.76	1.62	0.53
FeO	2.50	1.45	1.50	2.01	1.58	1.46	0.48
MnO	0.04	0.033	0.026	0.055	0.062	0.034	0.004
TiO_2	0.361	0.181	0.155	0.323	0.157	0.19	0.065
P_2O_5	0.11	0.07	0.05	0.07	0.06	0.08	0.02
LOI	0.32	0.35	0.25	0.32	0.63	0.46	0.45
Sum	100.36	100.46	100.19	100.18	100.28	99.77	100.4
V	37.16	19.72	9.46	28.88	8	14	null
Co	2	2	1	3	6	1	2
Ni	null	null	null	null	55	23	null
Cu	35.49	16.02	null	11.73	null	null	10
Zn	77	null	44	null	50	41	null
Ga	21.63	20.32	20.95	18.62	21	22	10
Rb	272.01	318.62	326.67	427.52	444	236	190
Sr	402.42	235.71	121.48	381.68	144	336	97
Y	48.30	18.93	14.64	18.76	18.2	10.2	13.8
Zr	326.23	157.77	155.65	256.74	131	124	73
Nb	19.85	15.41	5.08	22.39	22	5.1	5.8
Ba	1140	790.13	391.68	1200	376	830	392
La	81.64	32.46	42.71	66.54	60.1	40.9	29.2
Ce	139	51.92	73.04	100.75	105	67.6	48.3
Pr	16.9	5.77	8.57	10.77	12.4	7.57	5.28
Nd	59.81	19.17	28.96	33.62	41.2	25.8	18

Table 2. (continued)

	99-5-4-2	99-5-9-3	99-5-11-2	ND-4-00	BD-3-00	BD-7-00	BD-8-00
Sm	9.58	3.58	5.61	3.60	7.15	3.87	3.06
Eu	1.34	0.59	0.61	0.94	0.573	0.78	0.44
Gd	7.8	3.68	4.96	2.69	6.01	3.16	2.35
Tb	1.11	0.64	0.69	0.39	0.82	0.38	0.39
Dy	6.62	3.58	3.05	2.52	3.71	1.85	2.28
Ho	1.47	0.64	0.49	0.54	0.6	0.33	0.46
Er	4.72	1.57	1.25	1.83	1.57	0.94	1.51
Tm	0.85	0.22	0.18	0.32	0.248	0.129	0.254
Yb	5.34	1.26	1.10	2.08	1.6	0.85	1.77
Lu	0.67	0.17	0.16	0.30	0.236	0.128	0.281
Th	95.5	25.50	34.10	41.58	62.39	28.59	17.8
Pb	22.91	18.65	39.44	5.24	39.72	30.02	null
U	14.21	16.23	7.84	4.41	10.27	4.44	3.68
	99-5-5-4d	99-5-7-2A	99-5-7-3b	99-5-9-4A	99-5-11-1A	99-7-26-1b	ND-3-00
SiO_2	70.7	77.5	74.7	79.9	68.9	76.5	69.1
Al_2O_3	14.0	12.3	13.9	11.3	15.6	12.9	15.0
C_aO	1.54	0.32	1.2	1.24	2.3	0.59	2.08
MgO	0.45	0.03	0.19	0.17	1.04	0.27	0.98
Na_2O	3.91	3.82	3.78	3.43	4.22	2.84	3.28
K_2O	4.32	4.63	4.52	2.54	3.25	4.24	4.49
Fe_2O_3	2.17	1.25	1.46	1.46	2.92	1.66	3.38
FeO	1.95	1.12	1.31	1.31	2.63	1.49	3.04
MnO	0.085	0.017	0.038	0.021	0.061	0.042	0.071
TiO_2	0.265	0.05	0.127	0.15	0.599	0.164	0.491
P_2O_5	0.09	0.01	0.04	0.03	0.2	0.17	0.17
LOI	1.71	0.29	0.32	0.22	0.4	0.94	0.95
Sum	99.23	100.22	100.27	100.48	99.51	100.24	100.05
V	18	null	9	8	41	11	39
Co	71	2	null	null	58	101	75
Ni	null	null	null	null	22	null	null
Cu	null	null	null	null	23	null	null
Zn	null	null	null	34	61	41	63
Ga	16	16	14	14	25	20	19
Rb	203	266	210	164	352	415	244
Sr	168	20	134	73	517	62	334
Y	24.7	53.3	19.6	9.9	11	23	35.2
Zr	196	78	105	112	174	78	289
Nb	11.4	10.3	7	15.7	9.4	13.5	22
Ba	324	22	702	174	807	134	586
La	43.8	12.6	34.8	27.6	42.4	16.1	65.8
Ce	80.3	38.7	68.5	53.9	82.6	39	122
Pr	8.03	4.51	6.93	5.58	8.23	3.9	12.5
Nd	27.8	20.5	24.2	20.5	29.5	14.4	44.9
Sm	4.9	7.45	4.08	4.25	4.46	3.41	8.1
Eu	0.699	0.073	0.607	0.481	1.06	0.264	1.39
Gd	4.28	7.63	3.11	3.66	3.57	3.13	7.02
Tb	0.62	1.68	0.54	0.5	0.41	0.68	0.95
Dy	3.81	10.5	3.37	2.39	1.97	4.07	5.75
Ho	0.84	2.09	0.68	0.35	0.38	0.78	1.18
Er	2.58	6.37	2.18	0.77	1.08	2.24	3.52
Tm	0.412	1	0.343	0.09	0.176	0.368	0.545
Yb	2.69	6.26	2.34	0.46	1.15	2.33	3.6
Lu	0.4	0.858	0.337	0.049	0.175	0.314	0.523
Th	33.7	28.3	12.7	13.4	19.5	18.7	31.3
Pb	21	22	16	34	28	87	29
U	6.13	5.28	1.29	2.12	3.37	3.95	6.31
	ND-9-00	ND-13-00	ND-14-00b	ND-15-00	ND-22-00	YD-7-OOA	YD-8-OOB
SiO_2	67.2	53.6	75.2	68.3	77.0	71.9	73.6
Al_2O_3	16.6	16.8	13.8	15.5	12.2	14.5	13.8
C_aO	2.8	7.29	1.39	2.03	0.52	1.86	1.79
MgO	1	3.53	0.14	0.7	0.09	0.5	0.47
Na_2O	3.94	2.98	2.84	3.42	3.66	3.42	3.26
K_2O	3.91	4.39	5.78	5.5	3.77	5.26	4.75
Fe_2O_3	3.43	9.16	0.9	2.83	1.85	2.04	1.78
FeO	3.09	8.24	0.81	2.55	1.66	1.84	1.60
MnO	0.071	0.168	0.009	0.068	0.062	0.059	0.058
TiO_2	0.416	1.057	0.08	0.329	0.079	0.246	0.225
P_2O_5	0.18	0.58	0.04	0.12	0.03	0.08	0.07
LOI	0.87	0.72	0.25	0.47	0.88	0.46	0.54
Sum	100.44	100.31	100.45	99.24	100.08	100.35	100.31
V	35	204	9	28	null	22.43	17.54

Table 2. (continued)

	ND-9-00	ND-13-00	ND-14-00b	ND-15-00	ND-22-00	YD-7-OOA	YD-8-OOB
Co	4	18	2	3	null	2	2
Ni	null	34	20	null	null	29	null
Cu	null	23	null	null	null	null	null
Zn	55	65	null	46	48	35	null
Ga	22	20	15	18	17	15.82	14.15
Rb	186	203	218	278	221	199.29	188.22
Sr	423	750	281	334	57	238.66	207.38
Y	56.5	36	20.5	24	65.1	17.36	18.01
Zr	257	151	66	193	122	166.51	130.63
Nb	26.3	6.4	12.7	13.9	17.6	5.81	7.27
Ba	878	632	475	623	288	776.82	622.43
La	91.7	76.7	16.1	47.3	31.8	32.88	37.66
Ce	137	136	30.4	87.7	63.6	53.45	60.94
Pr	15.3	17.4	3.23	8.82	6.93	6.19	6.65
Nd	51.7	68.9	11.7	31.9	27.1	21.04	22.41
Sm	10	12.7	2.81	5.71	6.99	3.49	3.57
Eu	1.05	3.25	0.503	1.22	0.489	0.83	0.76
Gd	10.1	11.6	2.78	4.76	7.44	3.23	3.12
Tb	1.77	1.48	0.48	0.65	1.44	0.48	0.49
Dy	10	7.18	2.97	3.88	9.21	2.70	2.83
Ho	1.98	1.32	0.62	0.8	2.04	0.56	0.59
Er	5.41	3.36	1.97	2.48	6.77	1.65	1.75
Tm	0.898	0.431	0.312	0.383	1.05	0.27	0.30
Yb	5.57	2.83	2.24	2.51	6.94	1.87	2.02
Lu	0.757	0.394	0.366	0.388	1.06	0.30	0.32
Th	18.09	4.93	20.6	24.4	32.8	28.50	21.56
Pb	23.09	null	33	32	58	16.56	14.52
U	4.84	1.77	8.37	5.61	7.21	9.01	4.98
	YD-11-00	YD-13-OO	YD-33-OO	YD-37-OO	GL-1-00	GL-11-00	GL-12-00
SiO_2	76.3	74.6	72.7	76.8	65.5	77.4	74.5
Al_2O_3	12.8	13.4	14.5	12.7	15.5	11.8	12.9
C_aO	0.71	1.08	1.24	1.05	5.36	0.12	1.31
MgO	0.09	0.28	0.39	0.21	1.92	0.16	0.4
Na_2O	3.28	3.59	3.38	2.07	2.82	2.74	2.81
K_2O	5.07	4.98	5.07	5.18	2.4	5.43	4.98
Fe_2O_3	1.23	1.61	1.86	1.25	4.63	1.63	1.86
FeO	1.11	1.45	1.67	1.12	4.17	1.47	1.67
MnO	0.056	0.083	0.043	0.042	0.11	0.025	0.023
TiO_2	0.152	0.169	0.237	0.163	0.493	0.139	0.212
P_2O_5	0.03	0.05	0.06	0.04	0.15	0.04	0.09
LOI	0.68	0.26	0.73	0.59	1.56	0.98	1.14
Sum	100.42	100.17	100.19	100.02	100.44	100.47	100.21
V	6	6	11	7	92	null	16
Co	null	null	2	1	7	1	2
Ni	null	null	null	null	128	null	null
Cu	null	null	null	null	14	null	null
Zn	null	47	66	null	61	null	null
Ga	14	15	15	14	17	16	16
Rb	185	203	153	178	111	238	195
Sr	118	146	250	122	346	54	131
Y	22.4	23.7	24.8	21.1	21.6	47.4	30.7
Zr	123	130	170	124	151	139	122
Nb	5.8	7.6	6.9	6	6	7.5	6.4
Ba	508	531	1350	863	479	459	538
La	32.6	30.1	64.4	62.2	41.3	54.8	29.3
Ce	61.3	50.6	98.5	99.1	67.4	98.9	50.3
Pr	5.9	5.89	10.8	11.2	7.84	12.6	6.08
Nd	20	21.3	36.5	37	27.4	46.9	22
Sm	3.35	4.06	5.41	5.39	4.68	9.14	4.3
Eu	0.676	0.788	1.24	0.901	1.18	0.831	0.849
Gd	3.19	3.82	4.96	4.83	4.63	8.88	4.59
Tb	0.55	0.64	0.74	0.66	0.69	1.45	0.8
Dy	3.22	3.77	3.95	3.54	3.84	8.1	4.72
Ho	0.7	0.77	0.81	0.69	0.79	1.66	1.02
Er	2.16	2.29	2.41	2.07	2.2	4.55	2.84
Tm	0.372	0.379	0.381	0.316	0.329	0.739	0.466
Yb	2.6	2.57	2.63	2.13	2.15	4.57	3.04
Lu	0.392	0.385	0.407	0.318	0.326	0.655	0.45
Th	20.44	13.57	15.85	27.10	25.72	33.67	23.95
Pb	16.34	15.69	10.94	15.87	18.54	13.58	12.73
U	3.00	3.14	2.79	2.94	3.91	3.39	3.85

Table 2. (continued)

	202–20	202–22	202–33
SiO_2	71.7	55.6	50.5
Al_2O_3	14.7	17.9	18.0
C_aO	1.23	6.65	7.98
MgO	0.47	3.35	4.32
Na_2O	3.6	3.73	3.22
K_2O	5.03	1.98	1.61
Fe_2O_3	2.09	8.01	9.61
FeO	1.88	7.21	8.65
MnO	0.051	0.131	0.133
TiO_2	0.292	1.141	1.205
P_2O_5	0.08	0.37	0.42
LOI	1.06	1.45	2.75
Sum	100.33	100.25	99.74
V	12	134	189
Co	115	50	44
Ni	null	41	40
Cu	null	15	24
Zn	null	60	102
Ga	15	2	21
Rb	174	66	56
Sr	249	863	926
Y	29.3	25.8	27.1
Zr	215	377	325
Nb	6.2	4.4	3.5
Ba	1300	659	446
La	57.8	32.4	26.7
Ce	91	57.6	null
Pr	10.4	7.81	7.38
Nd	35.3	32.5	32
Sm	5.53	6.19	6.43
Eu	1.26	2.07	2.16
Gd	5.01	6.01	6.29
Tb	0.77	0.86	0.92
Dy	4.5	4.66	4.96
Ho	0.93	0.94	0.97
Er	2.72	2.58	2.66
Tm	0.441	0.371	0.384
Yb	2.94	2.53	2.51
Lu	0.428	0.387	0.377
Th	22.02	10.28	6.09
Pb	12.34	null	5.88
U	12.93	2.55	1.39

[a]Major elements are in wt %, and trace elements are in ppm.

period or a primary ion beam that overlapped zones that grew during distinct magmatic or recrystallization episodes, we examined BSE and CL images. In samples that show age ranges of several million years, it is common to see textures consistent with partial resorption and reprecipitation (in the form of irregular boundaries between zones), or metamorphic overgrowths (Figure 8). Grains often have thin, CL-bright rims that reflect the youngest ages with the lowest Th/U. Monazites often display patchy zoning that are most likely associated with episodic dissolution/reprecipitation (Figure 8) [*Ayers et al.*, 1999; *Townsend et al.*, 2000].

5. Petrology and Geochemistry of Nyainqentanglha Granitoids

[36] Petrological descriptions of the granitoid rocks of the NQTL massif are given by *Kapp* [2004]. Metamorphic rocks of the NQTL massif were examined by *Harris et al.* [1988c], who obtained pressure and temperature conditions of 700° ± 70°C and 5.1 ± 2.5 kbar for a garnet-sillimanite xenolith within the NQTL orthogneiss ~50 km southwest of Damxung (Foldout 1) and 610° ± 70°C and 5.0 ± 1.3 kbar for a staurolite-garnet schist north of Damxung.

[37] We conducted garnet+biotite thermometry [*Ferry and Spear*, 1978; *Berman*, 1990] and garnet+biotite+muscovite+plagioclase barometry [*Hoisch*, 1990] from a sample of mylonitic gneiss (99-5-16-2a, Foldout 1) within the NSZ yielding a temperature of ~550°C and pressures of ~3.5 kbars (calculated for coupled garnet rim and adjacent matrix biotite). Assuming that recrystallization accompanied granitoid intrusion, a reasonable assumption given the high (>80%) degree of granitoid emplaced into the massif in the late Tertiary (Foldout 1), this datum suggests that the present exposure was exhumed from between about 12 to 15 km depth. The garnet is chemically homogeneous; garnet+biotite thermometry for a biotite inclusion and adjacent garnet composition within this garnet sample yields a temperature of 560° ± 50°C, consistent with the rim temperature.

[38] The orthogneiss host of the injection complex in Goring La valley contains andalusite, believed to be the result of contact metamorphism from the emplacement of the Late Miocene magmas. The gneiss also contains minor

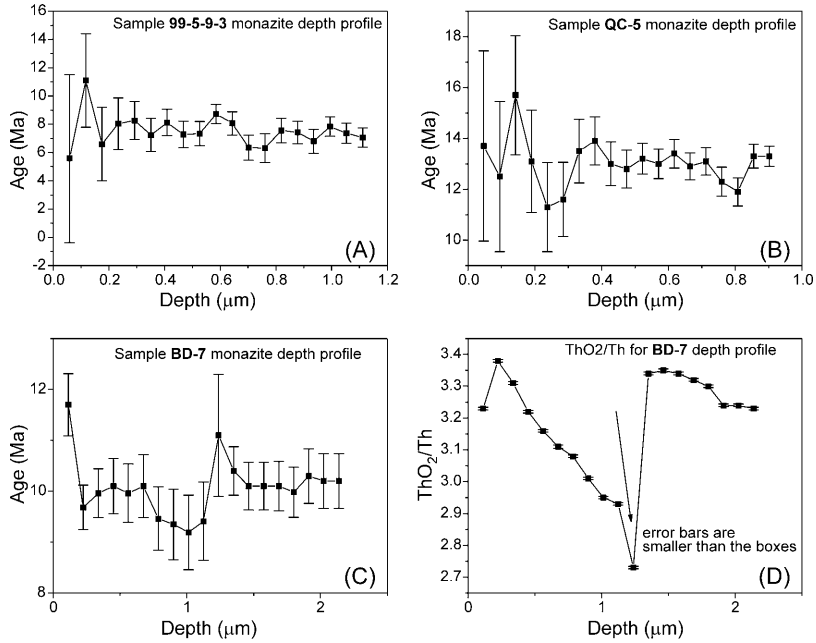

Figure 7. Results from three separate, single crystal monazite depth profiles. (a) Sample 99-5-9-3 from Goring La valley. No significant age variation is seen. (b) Sample QC-5 from Goring La valley. Again, no significant age variation is seen. (c and d) Sample BD-7 from Balum Chun La valley. Again, no significant age variation is seen. Notice where there is a slight jump in age, it corresponds to a drop in ThO_2/Th (see arrow in Figure 7d).

kyanite with what appears to be andalusite overgrowths, not previously documented in this area. Thus the presence of kyanite is interpreted to be a remnant of pre-Tertiary metamorphism.

[39] Granites of the NQTL massif are calc-alkaline in nature, have SiO_2 contents ranging from 50 to 80 weight percent, and are mainly peraluminous (Table 2). All of the Miocene granitoids are peraluminous ($Al_2O_3 > K_2O + Na_2O$ + CaO). The metaluminous samples examined include two granodiorites and one diorite that yield ages that correspond to the time range over which the Gangdese batholith was emplaced (ranging from 52 to 137 Ma).

[40] Major and trace element analyses were performed by XRAL Activation Services Inc., and Actlabs, using X-ray fluorescence (XRF), inductively coupled plasma mass spectrometry (ICP-MS), and instrumental neutron activation analysis (INAA). Major element abundances show a continuous, decreasing trend with increasing silica (Table 2). Trace element variation diagrams show scatter in both Rb and Ba concentrations with increasing fractionation (Table 2). Ba shows an inflection at ~70% silica, probably reflecting a saturation of potassium feldspar in the melt. Rb concentrations are unusually high for typical arc rocks (up to 630 ppm), perhaps indicating a lack of residual biotite. Zircon and monazite saturation temperatures [*Harrison and Watson*, 1983; *Rapp et al.*, 1987] indicate minimum temperatures of melting ranging up to 820°C (Table 3).

[41] Rare earth element (REE) data for granitoids of the NQTL complex (Table 2) show no significant variation in trace element abundances with age. Granitoids of all ages exhibit negative Eu anomalies. Most had Eu/Eu* values much less than 0.5, indicating only modest fractionation. Initial $^{87}Sr/^{86}Sr$ and ε_{Nd} data defined by all of the samples (Miocene and Gangdese age; Table A5 in the auxiliary material) fall on a mixing curve between the mantle array and crustal rocks characteristic of the Greater Himalayan Sequence rocks (Tibetan slab) or High Himalayan leucogranites (Figure 9). The range in initial $^{87}Sr/^{86}Sr$ values, most notably for the Miocene granitoids, suggests open-system processes and/or heterogeneous source rocks. Overall it appears that all granitoids of the NQTL were generated in an analogous fashion from similar source regions.

6. Thermochronology and Thermokinematic Modeling

[42] In light of our geological observations, we undertook new $^{40}Ar/^{39}Ar$ measurements to extend the results of *Harrison et al.* [1995] and new thermal modeling to more rigorously address the possibility of motion at low angle. Age spectra for samples from both Goring La and Balum Chun show a progressive increase in age with increasing structural distance from the NQTL detachment fault [*Harrison et al.*, 1995] (Figure 10). The $^{40}Ar/^{39}Ar$ thermal history results from these samples revealed the initiation of a rapid cooling event (i.e., slip on the NQTL detachment fault) at ~8 Ma. *Harrison et al.* [1995] used numerical simulations in which the angle of the detachment was varied, and concluded that the isotopically derived thermal histories precluded motion at low angle (<40°). Consequently, it was proposed that the fault was active at a higher dip angle and was subsequently rotated back to its present-day low angle.

[43] We analyzed two additional potassium feldspar samples from the northwest side of the NQTL massif near the

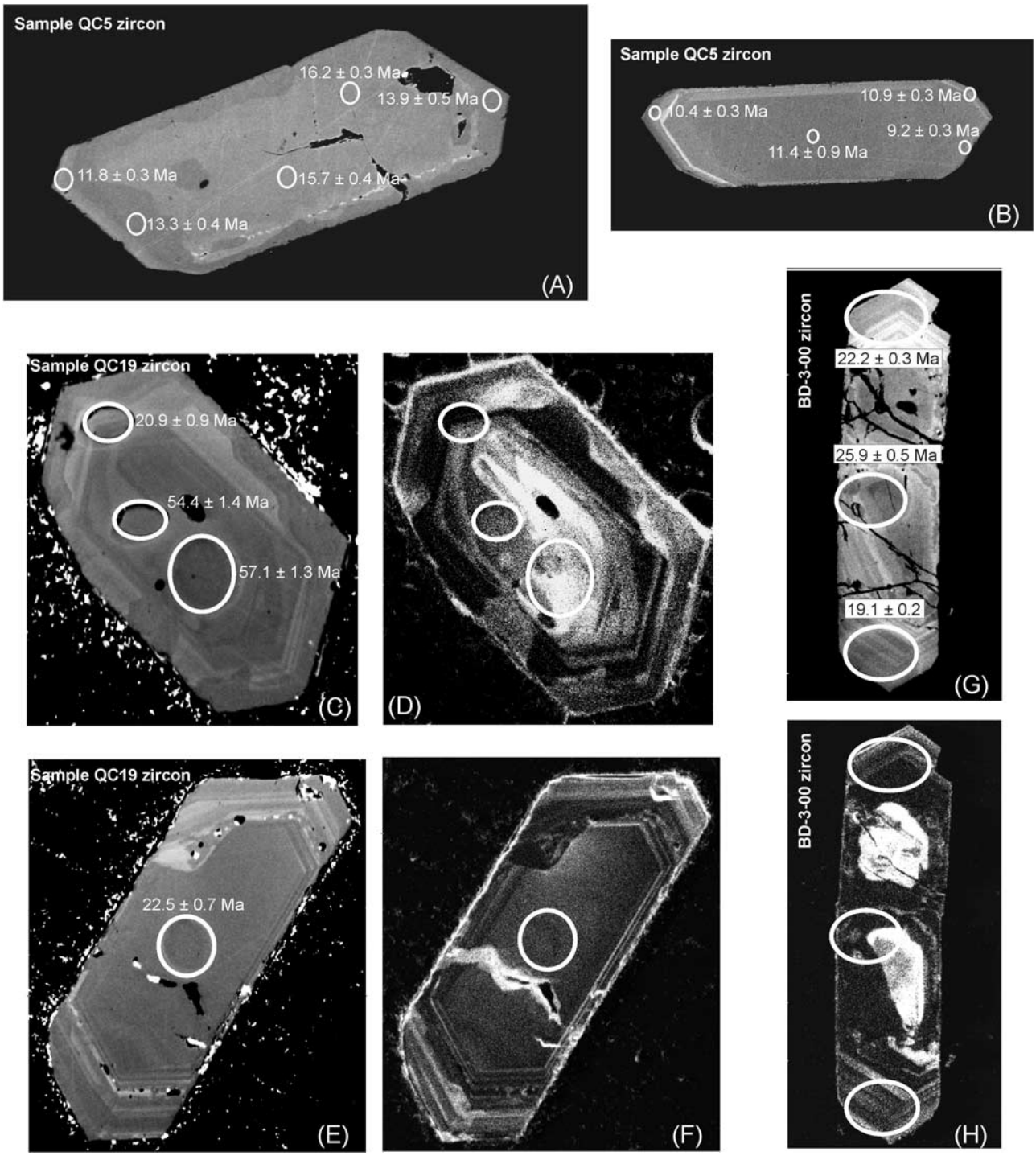

Figure 8. Backscattered electron (BSE) and cathodoluminescence (CL) images of zircons from granitoids of the Nyainqentanglha crystalline complex. White elliptical circles are ion probe analysis spots. (a) BSE image showing partial resorption textures and multiple age results. (b) Multiple age results (BSE). (c) BSE image showing partial resorption textures and complex age history (older core represents Gangdese arc formation while rim is younger). (d) CL image of same grain as in Figure 8c. (e) BSE image showing partial resorption texture, with core that corresponds in age to a major spike in zircon formation ages on summed probability plot (see Figure 7). (f) Same grain as Figure 8e in CL. (g) BSE image showing complex textures and age variation. (h) Same grain as Figure 8g in CL.

Table 3. Calculated Zircon and Monazite Saturation Temperatures

Sample	Zircon Saturation Temperature, °C	Monazite Saturation Temperature, °C
QC4	669.5	690.3
QC5	643.4	696.5
QC14	814.9	840.7
QC17	753.1	776.5
QC18	738.0	764.4
QC19	730.1	755.3
99-5-2-1A	722.7	750.8
99-5-4-2	737.8	754.9
99-5-5-4c	766.7	786.5
99-5-5-4d	782.8	739.8
99-5-7-2A	719.5	772.6
99-5-7-3b	739.4	801.4
99-5-9-4A	754.5	757.1
99-5-11-1A	774.5	787.3
99-5-11-2	752.7	761.4
99-7-26-1b	737.1	730.2
ND-3-00	819.8	821.8
ND-4-00	708.6	743.2
ND-14-00b	706.3	717.9
ND-15-00	776.6	794.2
ND-22-00	762.0	773.8
BD-3-00	763.5	787.5
BD-7-00	697.7	718.5
BD-8-00	754.7	798.6

Balum Chun La traverse (samples ND-3 and ND-4 on Foldout 1 and Table A6 in the auxiliary material). Their age spectra extend to progressively higher ages with increasing structural distance from the NQTL detachment fault (Figure 10). The $^{40}Ar/^{39}Ar$ age spectra of these two samples were interpreted both in terms of monotonic cooling and allowing for transient heating. Histories calculated assuming monotonic cooling fit well while those allowing for reheating alone do not, providing evidence that neither experienced a Miocene thermal excursion. Unfortunately, the calculated thermal histories from the two additional samples do not decisively distinguish between the two possibilities of movement at high angle and subsequent rollback or motion on a low-angle fault, due to limitations of the simple thermokinetic model employed by *Harrison et al.* [1995].

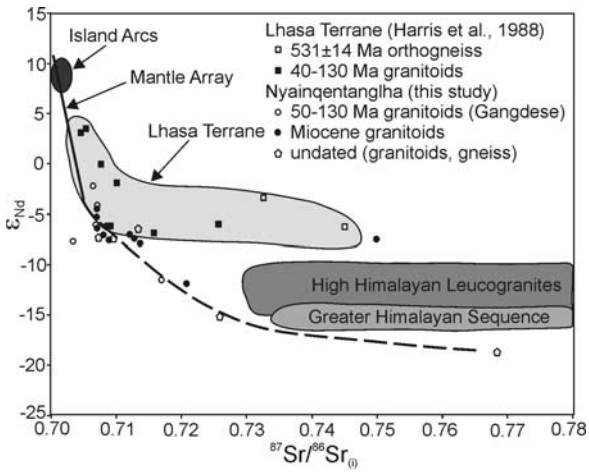

Figure 9. Epsilon Nd versus initial $^{87}Sr/^{86}Sr$ for Nyainqentanglha granitoids and related rocks. The field for the Lhasa terrane is as defined by *Harris et al.* [1988c]. Cretaceous and Miocene granitoids of the NQTL crystalline complex generally lie on a mixing trend (dashed line) between the mantle array and the fields of Greater Himalayan Crystallines (Tibetan slab) and High Himalayan leucogranites [*France-Lanord and Le Fort*, 1988].

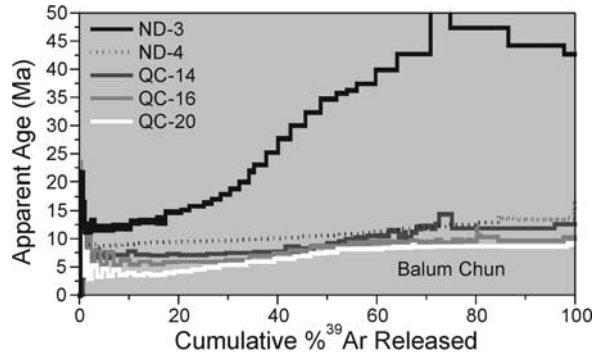

Figure 10. Previously and newly determined $^{40}Ar/^{39}Ar$ age spectra for Nyainqentanglha granitoids from Balum Chun valley. The progressive age increase with structural distance from the NQTL detachment fault led *Harrison et al.* [1995] to propose the rolling hinge model for the evolution of NQTL massif.

[44] In order to explain the overall field relationships and thermal history results across the NQTL rift system, a new thermokinematic model was developed using a "ramp-flat" geometry, in which the low-angle fault near the surface becomes higher angle in the upper crust and soles into a flat at ~12 km depth (Figure 11). This geometry seems to be reasonable for a fault in which rocks of the shear zone display textures consistent with formation near the brittle-ductile transition. This model was run for both a 45° and 30° dipping ramp, and corresponding thermal histories were extracted for six locations along the shear zone. Interestingly, this model produces the same form of age spectra as seen in the NQTL samples (Figure 11b). In general, the six samples experience very different temperature-time histories, which is the observation we were trying to reproduce. We note that the results of modeling of thermal histories are not unique, and magmas have not been introduced into the system during faulting. It is clear from the detailed geochronology of the NQTL massif that magmatism between 24 and 8 Ma played a large role in its thermal evolution, and ignoring magma input detracts from the applicability of the thermal models. One way of eliminating the problem of getting similar thermal histories for samples at opposite ends of the valleys [see *Harrison et al.*, 1995] would be to introduce high-temperature melts at depth, thereby influencing the deepest (i.e., closest to the fault) samples. Modeling motion on the NSZ, coupled with input of high-temperature magmas at intervals, would provide useful insights into the validity of the extent of rotation experienced by the NSZ, and requires further exploration.

7. Discussion

7.1. State of the Lhasa Block Middle Crust During the Miocene

[45] Observations from the NQTL massif provide insights into the deformational history of the Lhasa block. A key

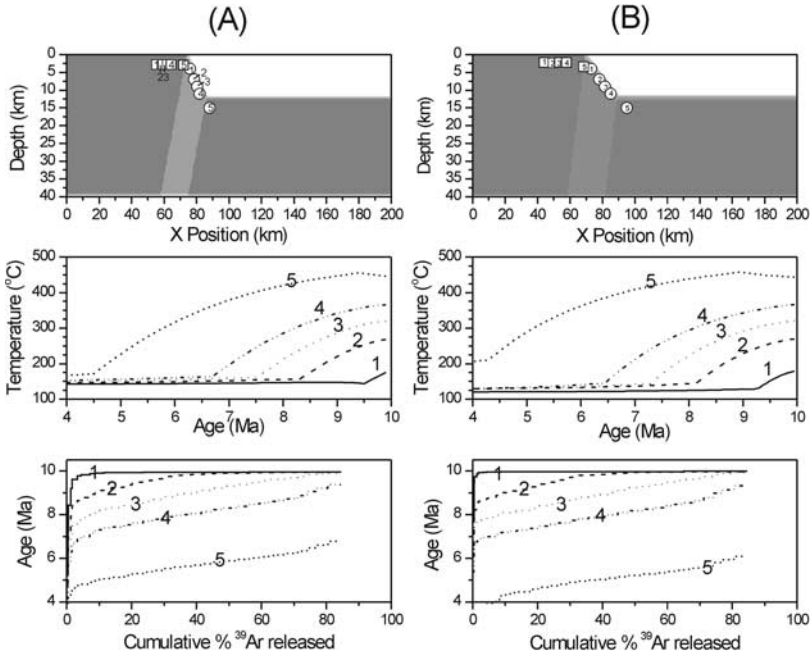

Figure 11. Thermokinematic modeling results for motion on a (a) 45° and (b) 30° fault. Model uses a normal geothermal gradient (25°C/km) and rate of motion of ~3 mm/year as estimated by *Harrison et al.* [1995]. Thermal histories and age spectra for both fault angles show the desired spread, as seen in Nyainqentanglha granitoid samples. Numbers 1–6 are initial (circles) and final (squares) sample locations as selected for the model.

question that we addressed in this study was what are the nature of the contacts between the crystalline rocks of the NQTL massif and the Paleozoic-Cretaceous metasedimentary rocks? In our studies of Goring La, Balum Chun, and other valleys transected from the northwest side of the NQTL range, we typically found sharp, and relatively undeformed intrusive contacts and a paucity of migmatitic fabrics in the wall rocks (Foldout 1). Our observation that both Miocene plutonic rocks and Cretaceous elements of the Gangdese batholith were brought to the surface in an essentially undeformed state during the Miocene is not supportive of models involving large-scale north-south flow in the middle to upper crust in southern Tibet [e.g., *Nelson et al.*, 1996; *Beaumont et al.*, 2001; *Hodges et al.*, 2001; *Grujic et al.*, 2002]. The lack of migmatites (in situ partial melts) in the exposed NQTL detachment fault footwall also argues against an extensive partial melt zone in the 12- to 15-km depth range of the Tibetan crust.

7.2. Late Cenozoic Structural Evolution

[46] Precise estimates for the magnitude of late Cenozoic extension across the NQTL massif and Yangbajain-Damxung graben are difficult to determine due to the lack of well defined hanging wall and footwall cutoffs (see cross sections in Foldout 1). However, an important observation is that the NQTL shear zone foliation is distinguishable along the upper parts of ridges along the southeastern flank of the NQTL massif with dip slopes that are oriented subparallel to the foliation. Along the central part of the massif, the shear zone can be traced continuously along these ridges from elevations in excess of 6 km southeastward to the range front over a down-slope distance of ~8 km (Foldout 1). This observation provides a robust minimum slip estimate (~8 km) for the NQTL detachment fault. The presence of rocks that equilibrated at a depth of 12–15 km directly beneath the detachment fault (see section 5) near Nyinzhong (Foldout 1) requires that the cumulative throw along all normal faults at this locale was 12–15 km. This equates to a cumulative displacement of 14–17 km along high-angle (60°) normal faults or 21–26 km along the NQTL detachment fault. Note that the latter estimate assumes a dip of 35° and that the high-angle normal faults root into the detachment fault at depth.

[47] The magnitude of late Cenozoic extension across the NQTL rift system appears to decrease to the northeast away from the central segment near Yangbajain. This inference is based on a northeastward decrease in the extent of footwall exhumation as indicated by (1) a northeastward decrease in width of the NQTL massif from up to 46 km wide along the Goring La traverse to as narrow as ~23 km northwest of Damung and (2) the observation that exposures of Miocene granitoids are widespread in the central part of the range but absent to the northeast (Foldout 1).

[48] The rolling-hinge model [e.g,. *Wernicke and Axen*, 1988; *Axen and Bartley*, 1997] has been used to explain the late Cenozoic structural and thermal evolution of the NQTL extensional system [*Harrison et al.*, 1995; *Cogan et al.*, 1998]. In this model, active normal faulting is at all stages during the evolution accommodated in the upper crust by a high-angle normal fault that is listric at depth. Isostatic rebound of the footwall during normal faulting results in rotation of the footwall in the opposite direction of normal fault displacement and the abandonment of older, structurally higher normal faults that have been rotated to low angles along with the footwall.

[49] If the rolling hinge model is valid for the NQTL extensional system, then the NQTL detachment fault should steepen to high angle at depth directly beneath the surface trace of southeast dipping high-angle normal faults along the southeastern flank of the NQTL massif (Foldout 1). However, seismic reflection studies suggest that the Nyainqentanglha detachment fault extends to depth at a low angle beneath the graben and is not significantly disrupted by high-angle normal faults to the southeast [*Cogan et al.*, 1998]. This finding requires that the high-angle normal faults within the Yangbajain-Damxung graben sole at depth and feed slip into the NQTL detachment fault as shown in the cross sections of *Cogan et al.* [1998].

[50] Active slip on the NQTL detachment fault in the upper crust is consistent with the surface geology. If extension across the NQTL rift system was in large part accommodated by slip along high-angle faults within the graben, those within the central part of the rift should have a greater cumulative throw than those to the northeast to explain the apparent northeastward decrease in the magnitude of extension. We would expect this to be reflected by greater offset and rotation of the NQTL detachment fault in the footwalls of the southeast dipping normal faults along the central part of the range than to the northeast. However, the NQTL detachment fault is consistently low-angle and exposed at similar elevations (4500–4800 m) and structural levels (with respect high-angle normal faults to the southeast) along the entire length of the range shown in Foldout 1. Furthermore, if the NQTL detachment fault was active only at a high angle in the upper crust but was subsequently rotated to lower angle in the footwalls of younger high-angle normal faults, then structurally underlying rocks should have rotated along with the detachment fault.

[51] We suggest that dikes in the injection complex of Goring La valley record the orientation of σ_1 at the time of their emplacement (Figure 2). One of these dikes yielded an age of 8.7 Ma, similar to the age of normal fault initiation. This orientation is vertical, the same as that which characterizes the present-day orientation of stress in the upper crust [e.g., *Mercier et al.*, 1987; *Ratschbacher et al.*, 1994]. Hence the orientation of the dikes suggests that this part of the footwall did not experience any significant finite rotation during extension.

[52] The geometry of NQTL rift basin fill may provide additional insight into the structural style of extension. Half-graben systems bounded by high-angle normal faults are generally associated with deep (>5 km) rift basin fill that thickens substantially toward the footwall [e.g., *Leeder and Gawthorpe*, 1987; *Friedmann and Burbank*, 1995]. In contrast, extensional basins that form in highly extended terrains above low-angle normal faults are generally characterized by thin (<3 km) basin fill and depocentres which are distal to range front low-angle normal faults [*Friedmann and Burbank*, 1995]. The NQTL rift basin is strikingly similar to the latter, being characterized by thin basin fill (<1500 m) which thickens southeastward away from the range front NQTL detachment fault [*Cogan et al.*, 1998].

[53] While the NQTL detachment fault may be presently active at low-angle in the upper crust, we suggest that extension was initially accommodated by a high-angle normal fault system. This is based on the observation that every other rift documented on the Tibetan plateau is bounded by high-angle normal faults, including the northern (Gulu; Figure 1) and southern (Foldout 1) extensions of the NQTL rift system [e.g., *Armijo et al.*, 1986; *Mercier et al.*, 1987; *Ratschbacher et al.*, 1994; *Yin et al.*, 1999a; *Blisniuk et al.*, 2001; *Taylor et al.*, 2003]. Presumably, extension is initially accommodated in the upper crust by high-angle listric normal faults that lead to the development of a detachment fault system with increasing displacement. How this may occur kinematically and mechanically is addressed at length by *Davis and Lister* [1988] and *Lister and Davis* [1989]. Figure 12 is a schematic kinematic model that may be applicable to the NQTL rift system in specific. Normal faulting initiates on a high-angle, listric normal fault that feeds slip into a mylonitic shear zone in the midcrust (Figure 12a). Tectonic unloading results in isostatic rebound of the footwall, rotation and eventual abandonment of the upper part of the high-angle normal fault (referred to as "breakaway 1"), and upwarping of the normal fault in the middle-upper crust (Figure 12b). A second high-angle normal fault ("breakaway 2") propagates structurally upward from near the upwarped portion of the normal fault at depth into the hanging wall of breakaway 1 (Figure 12b). Progressive development of breakaway normal faults and upwarping of, but continued slip along the normal fault at depth results in the present-day configuration in which active, southeast dipping high-angle normal faults along the northwestern margin of the Yangbajain-Damxung rift represent the youngest "breakaway zone" and feed slip into a detachment fault at depth (Figure 12c). Note that the older breakaway faults (and possible associated half-graben basins) are entirely eroded due to footwall uplift. NQTL rift basin fill only records the development of the youngest breakaway faults and is characteristic of that which is deposited above an active low-angle normal fault [*Friedmann and Burbank*, 1995]. Rocks on the northwest flank of the NQTL massif are rotated to a northwest dip, consistent with the regional northwest dip of the unconformity beneath Upper Cretaceous red beds along this part of the range (Foldout 1). The NQTL shear zone, presently exposed along the southeastern flank of the NQTL massif, underwent minimal rotation in the brittle upper crust during extension.

7.3. Origin of Miocene Magmatism

[54] A model for generation of the abundant Miocene magmas of the NQTL massif needs to accommodate the following observations: (1) the high-temperature (minimum temperatures up to 820°C) nature of the melts (Table 3), and (2) the isotopically mixed nature of the melts, requiring input from a juvenile source and a radiogenic crustal component (Figure 9). Given that the Moho temperature beneath southern Tibet is estimated to be <750°C [*Ruppel and McNamara*, 1997], the first constraint introduces the need for an external heat source. The second constraint implies that there was chemical contribution from either mantle melts, or perhaps underplated oceanic material, left at the lithospheric base of the Lhasa block from closure of the Tethys ocean.

[55] Upwelling of mantle derived melts into the lower crust of the Lhasa block would provide both the heat source and the chemistry required to generate the NQTL melts.

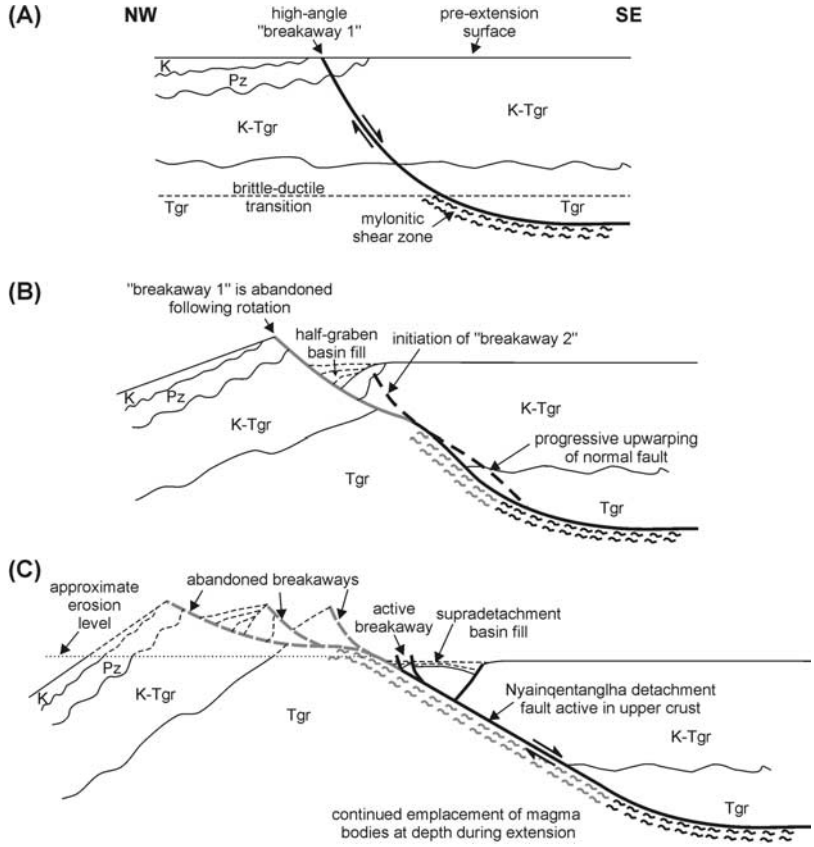

Figure 12. Schematic cross-sectional model for the late Cenozoic extensional evolution of the NQTL massif and rift system. (a) Initial extension is accommodated by slip along a SE dipping listric normal fault that is high angle in the upper crust (''breakaway 1'') and soles at depth into a subhorizontal mylonitic shear zone. (b) Isostatic rebound of the footwall during tectonic unloading upwarps and decreases the dip of the normal fault. Slip continues along the lower angle fault at depth but is fed to the surface along a new high-angle normal fault (''breakaway 2'') in the hanging wall of the now inactive ''breakaway 1.'' (c) Present-day configuration following additional extension, footwall isostatic rebound, breakaway zone development, and footwall erosion. The NQTL detachment fault is active in the upper crust. Older breakaway faults and possible associated basin fill have been uplifted and eroded. K, Cretaceous red beds; Pz, Paleozoic sedimentary rocks; K-Tgr, Cretaceous–early Tertiary Gangdese granite; Tgr, Miocene granite.

Recent results from seismic tomography indicate that the Indian plate has overridden its own sinking mantle [*Replumaz et al.*, 2004]. This scenario is capable of explaining why high-temperature (>800°C) calc-alkaline magmas have continued to be episodically emplaced along the trace of the Cretaceous–early Tertiary Gangdese batholith of southern Tibet ~50 Ma after closure of the Tethys ocean [*Honneger et al.*, 1982; *Schärer et al.*, 1984; *Xu et al.*, 1985; *Coulon et al.*, 1986; *Debon et al.*, 1986; *Xu*, 1990; *Miller et al.*, 1999; *Harrison et al.*, 2000; *Miller et al.*, 2000; *Williams et al.*, 2001; *Chung et al.*, 2003].

[56] There has been debate over the nature of Tibetan ''bright spots'' seen in seismic reflection profiles along the Yadong-Gulu rift, with several workers proposing that they represent widespread ponded crustal melts in the Tibetan middle crust. However, others have argued that they are actually hydrothermal fluids [*Makovsky et al.*, 1996; *Makovsky and Klemperer*, 1999], and the presence of active hydrothermal fields within the Yangbajain graben support this view. Studies of geothermal water within the Yangbajain graben reveal that they carry a resolvable ^{3}He anomaly consistent with a mantle contribution [*Yokoyama et al.*, 1999; *Hoke et al.*, 2000]. This observation supports our view that there is a contribution at depth from mantle-derived melts into the magmatic system of the NQTL massif. If indeed the bright spots are melts, this does not necessarily require a widespread, long-lived partial melt zone within the middle crust. The seismic studies were restricted to the rift systems, and therefore bright spots may reflect the geologic properties of the rifts only, and not be applicable to the whole of the Tibetan plateau, or even all of southern Tibet. Recent work by *Haines et al.* [2003] across the Bangong-Nuijang suture and the Qiangtang block does not show any evidence of bright spots, suggesting their limited extent. Using them as the basis for a large-scale midcrustal partial melt zone may be over zealous. Also, the episodic (~140–55 Ma, ~24–8 Ma) nature of the magmatic system for at least the last 140 Ma suggests that it may still be ongoing, and perhaps the bright spots are giving us a glimpse of the most recent

episode of magma emplacement, not a long-lived or voluminous melt layer.

7.4. Style of Cretaceous Deformation

[57] Perhaps the most striking feature of the exposed Cretaceous granitoids is their essentially undeformed nature. In contrast, the overlying Cretaceous strata in the region have been shortened by at least 40% [*Pan*, 1993; *Murphy et al.*, 1997]. The development of a fold-thrust belt within the Cretaceous strata, and lack of any brittle thrust faults or penetrative deformation in the Cretaceous granites, is difficult to explain. A possible explanation is that the upper crustal shortening was accommodated in the deeper crust by rigid-body northward underthrusting of the Lhasa terrane beneath the Qiangtang terrane during Cretaceous time [*Kapp et al.*, 2003, 2005]. This would permit the upper crust and supracrustal assemblages to deform extensively without penetratively deforming the Cretaceous granitoids of the middle crust.

8. Conclusions

[58] The exhumed footwall of the Nyainqentanglha massif provides a rare glimpse at a partial crustal section of the Lhasa block, southern Tibet. U-Th-Pb dating of zircon and monazite show the crystalline complex as largely a collage of granitoid intrusions of various ages, including many Cretaceous–early Tertiary granitoids of the Gangdese arc and Miocene granitoids. Emplacement ages of the latter span >10 m.y. (~24–8 Ma), suggesting semicontinuous or episodic magmatism. Miocene granites are reflective of calc-alkaline style magmatism, which continued after closure of the Tethys ocean and throughout the ongoing Cenozoic Indo-Asian collision. Miocene granitoids were generated from fairly high-temperature melts (calculated accessory mineral saturation temperatures >820°C), and geochemical and isotopic analyses reveal their similarity to rocks of the Gangdese arc. They also received significant mass and heat contributions from mantle melts. The undeformed nature of the Cretaceous and Miocene granitoids of the footwall rocks suggests that Mesozoic and Cenozoic deformation of the Lhasa block occurred in a ''thin-skinned'' style, being concentrated in supracrustal assemblages. This, coupled with the lack of migmatites exposed in the footwall of the NSZ, implies that at the level of granitoid emplacement, the middle crust was not mobile. This does not support models of continental injection, midcrustal flow, or shallow anatexis of southern Tibet. Structural analysis and geological observations are consistent with the NQTL detachment having evolved from an initially high-angle normal fault to a presently active low-angle normal fault. The $^{40}Ar/^{39}Ar$ thermochronologic studies of footwall K-feldspars reveal that samples collected within several kilometers below the detachment fault experienced cooling prior to emplacement of some of the youngest leucogranites (10–8 Ma), indicating that the background isothermal structure of the upper crust was little perturbed since ~15 Ma. A thermokinematic model using a ramp-flat geometry on both a 45° and 30° ramp shear zone indicates that the variation in thermal histories seen in footwall samples could be accomplished on a low-angle fault, and the heat input of magmas during extension would greatly enhance this effect. A scenario by which the Miocene melts are generated deep in the lower crust, and emplaced quickly to midcrustal levels, could explain seismic reflection results that reveal highly conductive areas in the middle crust, as these small pockets of melt would be semicontinuously emplaced in the middle crust, yielding the ''bright spots''. Alternatively, hydrothermal activity driven by recharging mafic magmatic systems could account for the bright spots seen in seismic profiles along the NQTL rift.

[59] **Acknowledgments.** This research was supported by the U.S. National Science Foundation grant EAR9909551 awarded to T. Mark Harrison and An Yin. Special thanks to Michael Taylor, Zhou Yong, and Daniel Stockli for assistance in the field, to An Yin for comments on earlier drafts, and to Lothar Ratschbacher, Nicholas Arnaud, and Isabelle Manighetti for incisive and constructive reviews.

References

Aitchison, J. C., A. M. Davis, Badengzhu, and H. Luo (2003), The Gangdese Thrust: A phantom structure that did not raise Tibet, *Terra Nova*, *15*, 155–162.

Allègre, C. J., et al. (1984), Structure and evolution of the Himalaya-Tibet orogenic belt, *Nature*, *307*, 17–22.

Alsdorf, D., L. Brown, K. D. Nelson, Y. Makovsky, S. Klemperer, and W. Zhao (1998), Crustal deformation of the Lhasa terrane, Tibet Plateau from Project INDEPTH deep seismic reflection profiles, *Tectonics*, *17*, 501–519.

Armijo, R., P. Tapponnier, J. L. Mercier, and T.-L. Han (1986), Quaternary extension in southern Tibet: Field observations and tectonic implications, *J. Geophys. Res.*, *91*, 13,803–13,872.

Argand, E. (1924), La tectonique de L'Asie, *Proc. Int. Geol. Congr. 13th*, *13*(7), 171–372.

Axen, G. J., and J. M. Bartley (1997), Field tests of rolling hinges: Existence, mechanical types, and implications for extensional tectonics, *J. Geophys. Res.*, *102*, 20,515–20,537.

Ayers, J. C., C. F. Miller, B. Gorisch, and J. Milleman (1999), Textural development of monazite during high-grade metamorphism: Hydrothermal growth kinetics, with implications for U, Th–Pb geochronology, *Am. Mineral.*, *84*, 1766–1780.

Beaumont, C., R. A. Jamieson, M. H. Nguyen, and B. Lee (2001), Himalayan tectonics explained by extrusion of a low-viscosity crustal channel coupled to focused surface denudation, *Nature*, *414*, 738–742.

Beaumont, C., R. A. Jamieson, M. H. Nguyen, and S. Medvedev (2004), Crustal channel flow: 1. Numerical models with applications to the tectonics of the Himalayan-Tibetan orogen, *J. Geophys. Res.*, *109*, B06406, doi:10.1029/2003JB002809.

Berman, R. G. (1990), Mixing properties of Ca-Mg-Fe-Mn garnets, *Am. Mineral.*, *75*, 328–344.

Bird, P. (1991), Lateral extrusion of lower crust from under high topography in the isostatic limit, *J. Geophys. Res.*, *96*, 10,275–10,286.

Blisniuk, P. M., B. R. Hacker, J. Glodny, L. Ratschbacher, S. Bi, Z. Wu, M. O. McWilliams, and A. Calvert (2001), Normal faulting in central Tibet since at least 13.5 Myr ago, *Nature*, *412*, 628–632.

Burg, J.-P., and G. M. Chen (1984), Tectonics and structural zonation of southern Tibet, China, *Nature*, *311*, 219–223.

Burg, J.-P., F. Proust, P. Tapponnier, and G. M. Chen (1983), Deformation phases and tectonic evolution of the Lhasa block (southern Tibet, China), *Eclogae Geol. Helv.*, *76*, 643–665.

Catlos, E. J., T. M. Harrison, C. E. Manning, M. Grove, S. M. Rai, M. S. Hubbard, and B. N. Upreti (2002), Records of the evolution of the Himalayan orogen from in situ Th-Pb ion microprobe dating of monazite: Eastern Nepal and western Garhwal, *J. Asian Earth Sci.*, *20*, 459–479.

Chang, C.-F., and S.-L. Zheng (1973), Tectonic features of the Mount Jolmu Lungma region in southern Tibet, China (in Chinese), *Sci. Geol. Sin.*, *1*, 1–12.

Cherniak, D. J., E. B. Watson, M. Grove, and T. M. Harrison (2004), Pb diffusion in monazite, *Geochim. Cosmochim. Acta*, *68*, 829–840.

Chung, S.-L., D. Liu, J. Ji, M.-F. Chu, H.-Y. Lee, D.-J. Wen, C.-H. Lo, T.-Y. Lee, Q. Qian, and Q. Zhang (2003), Adakites from continental collision zones: Melting of thickened lower crust beneath southern Tibet, *Geology*, *31*, 1021–1024.

Clark, M. K., and L. H. Royden (2000), Topographic ooze: Building the eastern margin of Tibet by lower crustal flow, *Geology*, *28*, 703–706.

Cogan, M. J. (1995), INDEPTH seismic refraction analysis of the Yadong-Gulu rift: Evidence for a fluid middle crust beneath southern Tibet, China, M.S. thesis, 74 pp., Syracuse Univ., Syracuse, N. Y.

Cogan, M. J., K. D. Nelson, W. S. F. Kidd, C. Wu, and Project INDEPTH Team (1998), Shallow structure of the Yadong-Gulu rift, southern Tibet, from refraction analysis of Project INDEPTH common midpoint data, *Tectonics*, *17*, 46–61.

Coleman, M. E., and K. V. Hodges (1995), Evidence for Tibetan plateau uplift before 14 m.y. ago from a new minimum age for east-west extension, *Nature*, *374*, 39–41.

Coulon, C., H. Maluski, C. Bollinger, and S. Wang (1986), Mesozoic and Cenozoic volcanic rocks from central and southern Tibet: ^{39}Ar-^{40}Ar dating, petrological characteristics and geodynamical significance, *Earth Planet. Sci. Lett.*, *79*, 281–302.

Coward, M. P., W. S. F. Kidd, Y. Pan, R. M. Shackleton, and H. Zhang (1988), Structure of the 1985 Tibet Geotraverse, Lhasa to Golmud, *Philos. Trans. R. Soc. London, Ser. A.*, *327*, 307–336.

Davis, G. A., and G. S. Lister (1988), Detachment faulting in continental extension: Perspectives from the Southwestern U. S. Cordillera, *Geol. Soc. Am. Spec. Pap.*, *218*, 133–159.

Davis, G. H., and S. J. Reynolds (1996), *Structural Geology of Rocks and Regions*, 2nd ed., 776 pp., John Wiley, Hoboken, N. J.

Debon, F., P. LeFort, S. M. F. Sheppard, and J. Sonet (1986), The four plutonic belts of the Transhimalaya-Himalaya: A chemical, mineralogical, isotopic and chronological synthesis along a Tibet-Nepal section, *J. Petrol.*, *27*, 219–250.

DeCelles, P. G., D. M. Robinson, J. Quade, T. P. Ojha, C. N. Garzione, P. Copeland, and B. N. Upreti (2001), Stratigraphy, structure, and tectonic evolution of the Himalayan fold-thrust belt in western Nepal, *Tectonics*, *20*, 487–509.

DeCelles, P. G., D. M. Robinson, and G. Zandt (2002), Implications of shortening in the Himalayan fold-thrust belt for uplift of the Tibetan Plateau, *Tectonics*, *21*(6), 1062, doi:10.1029/2001TC001322.

Dewey, J. F., and K. C. A. Burke (1973), Tibetan, Variscan, and Precambrian basement reactivation: Products of continental collision, *J. Geol.*, *81*, 683–692.

Dewey, J. F., R. M. Shackleton, C. Chengfa, and S. Yiyin (1988), The tectonic evolution of the Tibetan Plateau, *Philos. Trans. R. Soc. London, Ser. A*, *327*, 379–413.

Ducea, M. N., et al. (2003), Building the Pamirs: The view from the underside, *Geology*, *31*, 849–852.

Edwards, M. A., and L. Ratschbacher (2005), Seismic and aseismic weakening effects in transtension: Field and microstructural observations on the mechanics and architecture of a large fault zone in southeastern Tibet, in *High Strain Zones in Nature and Experiment*, edited by D. Bruhn and L. Burlini, *Geol. Soc. Spec. Publ.*, in press.

England, P. C., and G. A. Houseman (1988), The mechanics of the Tibetan Plateau, *Philos. Trans. R. Soc. London*, *326*, 302–319.

England, P. C., and G. A. Houseman (1989), Extension during convergence, with application to the Tibetan Plateau, *J. Geophys. Res.*, *94*, 17,561–17,579.

Fan, G., and T. Lay (2002), Characteristics of Lg attenuation in the Tibetan Plateau, *J. Geophys. Res.*, *107*(B10), 2256, doi:10.1029/2001JB000804.

Ferry, J. M., and F. S. Spear (1978), Experimental calibration of partitioning of Fe and Mg between biotite and garnet, *Contrib. Mineral. Petrol.*, *66*, 113–117.

Fielding, E. J., B. L. Isacks, M. Barazangi, and C. Duncan (1994), How flat is Tibet?, *Geology*, *22*, 163–167.

France-Lanord, C., and P. Le Fort (1988), Crustal melting and granite genesis during Himalayan collisional orogenesis, *Trans. R. Soc. Edinburgh Earth Sci.*, *79*, 603–621.

Friedmann, S. J., and D. W. Burbank (1995), Rift basins and supradetachment basins: Intracontinental extensional end-members, *Basin Res.*, *7*, 109–127.

Grove, M., and T. M. Harrison (1999), Monazite Th-Pb age depth profiling, *Geology*, *27*, 487–490.

Grujic, D., L. S. Hollister, and R. Parrish (2002), Himalayan metamorphic sequence as an orogenic channel: Insight from Bhutan, *Earth Planet. Sci. Lett.*, *198*, 177–191.

Hacker, B. R., E. Gnos, L. Ratschbacher, M. Grove, M. McWilliams, S. V. Sobolev, J. Wan, and W. Zhenhan (2000), Hot and dry deep crustal xenoliths from Tibet, *Science*, *287*, 2463–2466.

Hacker, B. R., P. Luffi, V. Lutkov, V. T. Minaev, L. R. Ratschbacher, A. E. Patino-Douce, M. N. Ducea, M. O. McWilliams, and J. Metcalf (2005), Near-ultrahigh pressure processing of continental crust: Miocene crustal xenoliths from the Pamir, *J. Petrol.*, in press.

Haines, S. S., S. L. Klemperer, L. Brown, G. Jingru, J. Mechie, R. Meissner, A. Ross, and Z. Wenjin (2003), INDEPTH III seismic data: From surface observations to deep crustal processes in Tibet, *Tectonics*, *22*(1), 1001, doi:10.1029/2001TC001305.

Harris, N. B. W., R. Xu, C. L. Lewis, and J. Chengwei (1988a), Plutonic rocks of the 1985 Tibet Geotraverse, Lhasa to Golmud, *Philos. Trans. R. Soc. London, Ser. A.*, *327*, 145–168.

Harris, N. B. W., T. J. B. Holland, and A. G. Tindle (1988b), Metamorphic rocks of the 1985 Tibet Geotraverse, Lhasa to Golmud, *Philos. Trans. R. Soc. London, Ser. A.*, *327*, 203–213.

Harris, N. B. W., R. Xu, C. L. Lewis, C. J. Hawkesworth, and Z. Yuquan (1988c), Isotope geochemistry of the 1985 Tibet Geotraverse, Lhasa to Golmud, *Philos. Trans. R. Soc. London, Ser. A.*, *327*, 263–285.

Harrison, T. M., and E. B. Watson (1983), Kinetics of zircon dissolution and zirconium diffusion in granitic melts of variable water content, *Contrib. Mineral. Petrol.*, *84*, 66–72.

Harrison, T. M., P. Copeland, W. S. F. Kidd, and A. Yin (1992), Raising Tibet, *Science*, *255*, 1663–1670.

Harrison, T. M., P. Copeland, W. S. F. Kidd, and O. M. Lovera (1995), Activation of the Nyainqentanglha shear zone: Implications for uplift of the southern Tibetan Plateau, *Tectonics*, *14*, 658–676.

Harrison, T. M., F. J. Ryerson, P. Le Fort, A. Yin, O. M. Lovera, and E. J. Catlos (1997), A Late Miocene-Pliocene origin for the central Himalayan inverted metamorphism, *Earth Planet. Sci. Lett.*, *146*, E1–E7.

Harrison, T. M., M. Grove, K. D. McKeegan, C. D. Coath, O. M. Lovera, and P. LeFort (1999), Origin and episodic emplacement of the Manaslu Intrusive Complex, central Himalaya, *J. Petrol.*, *40*, 3–19.

Harrison, T. M., A. Yin, M. Grove, O. M. Lovera, F. J. Ryerson, and X. Zhou (2000), The Zedong window: A record of superposed Tertiary convergence in southeastern Tibet, *J. Geophys. Res.*, *105*, 19,211–19,230.

Hodges, K. V. (2000), Tectonics of the Himalaya and southern Tibet from two perspectives, *Geol. Soc. Am. Bull.*, *112*, 324–350.

Hodges, K. V., J. M. Hurtado, and K. X. Whipple (2001), Southward extrusion of Tibetan crust and its effect on Himalayan tectonics, *Tectonics*, *20*, 799–809.

Hoisch, T. D. (1990), Empirical calibration of six geobarometers for the mineral assemblage quartz + muscovite + biotite + plagioclase + garnet, *Contrib. Mineral. Petrol.*, *104*, 225–234.

Hoke, L., S. Lamb, D. R. Hilton, and R. Poreda (2000), Southern limit of mantle-derived geothermal helium emissions in Tibet: Implications for lithospheric structure, *Earth Planet. Sci. Lett.*, *180*, 297–308.

Honneger, K., V. Dietrich, W. Frank, A. Gansser, M. Thöni, and V. Trommsdorf (1982), Magmatism and metamorphism in the Ladakh Himalayas (The Indus-Tsangpo suture zone), *Earth Planet. Sci. Lett.*, *60*, 178–194.

Hubbard, M. S., and T. M. Harrison (1989), $^{40}Ar/^{39}Ar$ age constraints on deformation and metamorphism in the Main Central Thrust zone and Tibetan slab, eastern Nepal Himalaya, *Tectonics*, *8*, 865–880.

Huerta, A. D., L. H. Royden, and K. V. Hodges (1998), The thermal structure of collisional orogens as a response to accretion, erosion and radiogenic heating, *J. Geophys. Res.*, *103*, 15,287–15,302.

Johnson, M. R. W. (2002), Shortening budgets and the role of continental subduction during the India-Asia collision, *Earth Sci. Rev.*, *59*, 101–123.

Jolivet, M., M. Brunel, D. Seward, Z. Xu, J. Yang, J. Malavieille, F. Roger, A. Leyreloup, N. Arnaud, and C. Wu (2003), Neogene extension and volcanism in the Kunlun fault zone, northern Tibet: New constraints on the age of the Kunlun Fault, *Tectonics*, *22*(5), 1052, doi:10.1029/2002TC001428.

Kapp, J. L. D. (2004), The Nyainqentanglha shear zone: A window into the tectonic, thermal and chemical evolution of the Lhasa block, southern Tibet, Ph.D. dissertation, Univ. of Calif., Los Angeles.

Kapp, P., and J. H. Guynn (2004), Indian punch rifts Tibet, *Geology*, *32*, 993–996.

Kapp, P., M. A. Murphy, A. Yin, T. M. Harrison, L. Ding, and J. Guo (2003), Mesozoic and Cenozoic tectonic evolution of the Shiquanhe area of western Tibet, *Tectonics*, *22*(4), 1029, doi:10.1029/2001TC001332.

Kapp, P., A. Yin, T. M. Harrison, and L. Ding (2005), Cretaceous-Tertiary shortening, basin development, and volcanism in central Tibet, *Geol. Soc. Am. Bull.*, in press.

Kidd, W. S. F., Y. Pan, C. Chang, M. P. Coward, J. F. Dewey, A. Gansser, P. Molnar, R. M. Shackleton, and Y. Sun (1988), Geological mapping of the 1985 Chinese-British Tibetan (Xizang-Qinghai) Plateau Geotraverse route, *Philos. Trans. R. Soc. London, Ser. A.*, *327*, 287–305.

Kind, R., et al. (2002), Seismic images of crust and upper mantle beneath Tibet: Evidence for Eurasian plate subduction, *Science*, *298*, 1219–1221.

Leeder, M. R., and R. L. Gawthorpe (1987), Sedimentary models for extensional tilt-block/half-graben basins, in *Continental Extensional Tectonics*, edited by M. P. Coward, J. F. Dewey, and P. L. Hancock, *Geol. Soc. London Spec. Publ.*, *28*, 139-152.

Leeder, M. R., A. B. Smith, and Y. Jixiang (1988), Sedimentology and palaeoenvironmental evolution of the 1985 Lhasa to Golmud Geotraverse, *Philos. Trans. R. Soc. London, Ser. A.*, *327*, 107–143.

Lister, G. S., and G. A. Davis (1989), The origin of metamorphic core complexes and detachment faults formed during Tertiary continental extension in the northern Colorado River region, U. S. A., *J. Struct. Geol.*, *11*, 65–94.

Liu, Q., Z. Wu, D. Hu, P. Ye, W. Jiang, Y. Wang, and H. Zhang (2004), SHRIMP U-Pb zircon dating on Nyainqentanglha granite in central Lhasa block, *Chin. Sci. Bull.*, *49*, 76–82.

Liu, Z. Q. C. (Compiler) (1988), Geologic map of the Qinghai-Xizang Plateau and its neighboring regions, scale 1:1,500,000, Chengdu Inst. of Geol. and Miner. Resour., Beijing.

Makovsky, Y., and S. L. Klemperer (1999), Measuring the seismic properties of Tibetan bright spots: Evidence for free aqueous fluids in the Tibetan middle crust, *J. Geophys. Res.*, *104*, 10,795–10,825.

Makovsky, Y., S. L. Klemperer, L. Ratschbacher, L. Brown, M. Li, W. Zhao, and F. Meng (1996), INDEPTH wide-angle reflection observation of *p*-wave-to-*s*-wave conversions from crustal bright spots in Tibet, *Science*, *274*, 1690–1691.

McCaffrey, R., and J. Nabelek (1998), Role of oblique convergence in the active deformation of the Himalayas and southern Tibet Plateau, *Geology*, *26*, 691–694.

Mercier, J. L., R. Armijo, P. Tapponnier, E. Carey-Gailhardis, and T.-L. Han (1987), Change from late Tertiary compression to Quaternary extension in southern Tibet during the India-Asia collision, *Tectonics*, *6*, 275–304.

Meyer, B., P. Tapponnier, L. Bourjot, F. Metivier, Y. Gaudemer, G. Peltzer, S. Guo, and Z. Chen (1998), Crustal thickening in Gansu-Qinghai, lithospheric mantle subduction, and oblique, strike-slip controlled growth of the Tibet Plateau, *Geophys. J. Int.*, *135*, 1–47.

Miller, C., R. Schuster, U. Klotzli, W. Frank, and F. Purtscheller (1999), Post-collisional potassic and ultrapotassic magmatism in SW Tibet: Geochemical and Sr-Nd-Pb-O isotopic constraints for mantle source characteristics and petrogenesis, *J. Petrol.*, *40*, 1399–1424.

Miller, C., R. Schuster, U. Klotzli, W. Frank, and B. Grasemann (2000), Late Cretaceous-Tertiary magmatic and tectonic events in the Transhimalaya batholith (Kailas area, SW Tibet), *Schweiz. Mineral. Petrog. Mitt.*, *80*, 1–20.

Mojzsis, S. J., and T. M. Harrison (2002), Establishment of a 3.83-Ga magmatic age for the Akilia tonalite (southern west Greenland), *Earth Planet. Sci. Lett.*, *202*, 563–576.

Molnar, P., and H. Lyon-Caen (1989), Fault plane solutions of earthquakes and active tectonics of the Tibetan Plateau and its margins, *Geophys., J. Int.*, *99*, 123–153.

Molnar, P., and P. Tapponnier (1978), Active tectonics of Tibet, *J. Geophys. Res.*, *83*, 5361–5375.

Molnar, P., P. England, and J. Martinod (1993), Mantle dynamics, the uplift of the Tibetan plateau, and the Indian monsoon, *Rev. Geophys.*, *31*, 357–396.

Murphy, M. A., A. Yin, T. M. Harrison, S. B. Dürr, Z. Chen, F. J. Ryerson, W. S. F. Kidd, X. Wang, and X. Zhou (1997), Did the Indo-Asian collision alone create the Tibetan plateau?, *Geology*, *25*, 719–722.

Nelson, K. D., et al. (1996), Partially molten middle crust beneath southern Tibet: Synthesis of project INDEPTH results, *Nature*, *274*, 1684–1688.

Owens, T. J., and G. Zandt (1997), Implications of crustal property variations for models of Tibetan Plateau evolution, *Nature*, *387*, 37–43.

Paces, J. B., and J. D. Miller (1993), Precise U-Pb age of Duluth Complex and related mafic intrusions, northeastern Minnesota: Geochronological insights into physical, petrogenetic, and tectonomagmatic processes associated with the 1.1 Ga mid-continent rift system, *J. Geophys. Res.*, *98*, 13,997–14,103.

Pan, Y. (1993), Unroofing history and structural evolution of the southern Lhasa terrane, Tibetan Plateau: Implications for the continental collision between India and Asia, Ph.D. thesis, 287 pp., Univ. at Albany, State Univ. of N. Y., Albany.

Pan, Y., and W. S. F. Kidd (1992), Nyainqentanglha shear zone: A late Miocene extensional detachment in the southern Tibetan Plateau, *Geology*, *20*, 775–778.

Pearce, J. A., and H. Mei (1988), Volcanic rocks of the 1985 Tibet Geotraverse: Lhasa to Golmud, *Philos. Trans. R. Soc. London, Ser. A.*, *327*, 169–201.

Powell, C. M., and P. J. Conaghan (1973), Plate tectonics and the Himalayas, *Earth Planet. Sci. Lett.*, *20*, 1–12.

Quidelleur, X., M. Grove, O. M. Lovera, T. M. Harrison, and A. Yin (1997), Thermal evolution and slip history of the Renbu-Zedong Thrust, southeastern Tibet, *J. Geophys. Res.*, *102*, 2659–2679.

Rapp, R. P., F. J. Ryerson, and C. F. Miller (1987), Experimental evidence bearing on the stability of monazite during crustal anatexis, *Geophys. Res. Lett.*, *14*, 307–310.

Ratschbacher, L., W. Frisch, C. Chen, and G. Pan (1992), Deformation and motion along the southern margin of the Lhasa block (Tibet) prior to and during the India-Asia collision, *J. Geodyn.*, *16*, 21–54.

Ratschbacher, L., W. Frisch, G. Liu, and C. Chen (1994), Distributed deformation in southern and western Tibet during and after the India-Asia collision, *J. Geophys. Res.*, *99*, 19,917–19,945.

Replumaz, A., H. Karason, R. D. van der Hilst, J. Besse, and P. Tapponnier (2004), 4-D evolution of SE Asia's mantle from geological reconstructions and seismic tomography, *Earth Planet. Sci. Lett.*, *221*, 103–115.

Royden, L. H. (1993), The steady-state thermal structure of eroding orogenic belts and accretionary prisms, *J. Geophys. Res.*, *98*, 4487–4507.

Royden, L. H. (1996), Coupling and decoupling of crust and mantle in convergent orogens: Implications for strain partitioning in the crust, *J. Geophys. Res.*, *101*, 17,679–17,705.

Royden, L. H., B. C. Burchfiel, R. W. King, E. Wang, Z. Chen, F. Shen, and Y. Liu (1997), Surface deformation and lower crustal flow in eastern Tibet, *Science*, *276*, 788–790.

Ruppel, C., and D. McNamara (1997), Seismic and rheological constraints on the thermal state of Tibetan plateau upper mantle: Implications for melt production, mantle delamination, and large-scale tectonics, *Eos Trans. AGU*, *78*, Fall Meet. Suppl., F535.

Schärer, U., R. Xu, and C. J. Allègre (1984), U-Pb geochronology of the Gangdese (Transhimalaya) plutonism in the Lhasa-Xigaze region, Tibet, *Earth Planet. Sci. Lett.*, *67*, 311–320.

Schmitt, A. K., M. Grove, T. M. Harrison, O. M. Lovera, J. Hullen, and M. Waters (2003), The Cobb Mountain-Geyser's magma system, California (part 1): U-Pb zircon ages, conditions of crystallization, and magma residence times, *Geochim. Cosmochim. Acta*, *67*, 3423–3442.

Schmitz, M. D., S. A. Bowring, and T. R. Ireland (2003), Evaluation of Duluth Complex anorthositic series (AS3) zircon as a U-Pb geochronological standard: New high-precision isotope dilution thermal ionization mass spectrometry results, *Geochim. Cosmochim. Acta*, *67*, 3665–3672.

Seeber, L., and J. G. Armbruster (1984), Some elements of continental subduction along the Himalayan front, *Tectonophysics*, *105*, 263–278.

Stockli, D. F., M. Taylor, A. Yin, T. M. Harrison, J. L. D'Andrea, P. Kapp, and L. Ding (2002), Late Miocene-Pliocene inception of E-W extension in Tibet as evidenced by apatite (U-Th)/He data, *Geol. Soc. Am. Abstr. Programs*, *34*, 411.

Tapponnier, P., et al. (1981), The Tibetan side of the India-Eurasia collision, *Nature*, *294*, 405–410.

Tapponnier, P., G. Peltzer, and R. Armijo (1986), On the mechanics of the collision between India and Asia, in *Collision Tectonics*, edited by J. G. Ramsay, M. P. Coward, and A. Ries, *Geol. Soc. London Spec. Publ.*, *19*, 115–157.

Tapponnier, P., X. Zhiqin, F. Roger, B. Meyer, N. Arnaud, G. Wittlinger, and Y. Jingsui (2001), Oblique stepwise rise and growth of the Tibet Plateau, *Science*, *294*, 1671–1677.

Taylor, M., A. Yin, F. J. Ryerson, P. Kapp, and L. Ding (2003), Conjugate strike-slip faulting along the Bangong-Nujiang suture zone accommodates coeval east-west extension and north-south shortening in the interior of the Tibetan Plateau, *Tectonics*, *22*(4), 1044, doi:10.1029/2002TC001361.

Townsend, K. J., C. F. Miller, J. L. D'Andrea, J. C. Ayers, T. M. Harrison, and C. D. Coath (2000), Low temperature replacement of monazite in the Ireteba granite, southern Nevada: Geochronological implications, *Chem. Geol.*, *172*, 95–112.

Unsworth, M., W. Wenbo, A. G. Jones, S. Li, P. Bedrosian, J. Booker, J. Sheng, D. Ming, and T. Handong (2004), Crustal and upper mantle structure of northern Tibet imaged with magnetotelluric data, *J. Geophys. Res.*, *109*, B02403, doi:10.1029/2002JB002305.

Vergne, J., G. Wittlinger, Q. Hui, P. Tapponnier, G. Poupinet, J. Mei, G. Herquel, and A. Paul (2002), Seismic evidence for stepwise thickening of the crust across the NE Tibetan plateau, *Earth Planet. Sci. Lett.*, *203*, 25–33.

Wang, Q., et al. (2001), Present-day crustal deformation in China constrained by Global Positioning System measurements, *Science*, *294*, 574–577.

Wei, W., et al. (2001), Detection of widespread fluids in the Tibetan crust by magnetotelluric studies, *Science*, *292*, 716–718.

Wernicke, B., and G. J. Axen (1988), On the role of isostasy in the evolution of normal fault systems, *Geology*, *16*, 848–851.

Willett, S. D., and C. Beaumont (1994), Subduction of Asian lithospheric mantle beneath Tibet inferred from models of continental collision, *Nature*, *369*, 642–645.

Williams, H., S. Turner, S. Kelley, and N. Harris (2001), Age and composition of dikes in southern Tibet: New constraints on the timing of east-west extension and its relationship to postcollisional volcanism, *Geol. Soc. Am. Bull*, *29*, 339–342.

Wu, Z., D. Hu, P. Ye, X. Zhao, and Q. Liu (2004), Thrusting of the North Lhasa block in the Tibetan Plateau, *J. Geol. Soc. China*, *78*(1), 246–259.

Xie, J., R. Gok, J. Ni, and Y. Aoki (2004), Lateral variations of crustal seismic attenuation along the INDEPTH profiles in Tibet from *Lg Q* inversion, *J. Geophys. Res.*, *109*, B10308, doi:10.1029/2004JB002988.

Xu, R. (1990), Geochronological study of granitoids and metamorphic rocks in Xizang, in *Metamorphic and Igneous Rocks in Xizang*, edited by G. Lui et al., pp. 287-321, Geol. Press, Beijing.

Xu, R.-H., U. Schärer, and C. J. Allègre (1985), Magmatism and metamorphism in the Lhasa block (Tibet): A geochronological study, *J. Geol.*, *93*, 41–57.

Yin, A. (2000), Mode of Cenozoic east-west extension in Tibet suggesting a common origin of rifts in Asia during the Indo-Asian collision, *J. Geophys. Res.*, *105*, 21,745–21,759.

Yin, A., and T. M. Harrison (2000), Geologic evolution of the Himalayan-Tibetan Orogen, *Annu. Rev. Earth Planet. Sci.*, *28*, 211–280.

Yin, A., T. M. Harrison, F. J. Ryerson, C. Wenji, W. S. F. Kidd, and P. Copeland (1994), Tertiary structural evolution of the Gangdese Thrust system, southeastern Tibet, *J. Geophys. Res.*, *99*, 18,175–18,201.

Yin, A., P. Kapp, M. A. Murphy, T. M. Harrison, M. Grove, L. Ding, X. Deng, and C. Wu (1999a), Significant late Neogene east-west extension in northern Tibet, *Geology*, *27*, 787–790.

Yin, A., T. M. Harrison, M. A. Murphy, M. Grove, S. Nie, F. J. Ryerson, W. X. Feng, and C. Z. Le (1999b), Tertiary deformation history of southeastern and southwestern Tibet during the Indo-Asian collision, *Geol. Soc. Am. Bull.*, *111*, 1644–1664.

Yokoyama, T., S. Nakai, and H. Waikita (1999), Helium and carbon isotopic compositions of hot spring gases in the Tibetan Plateau, *J. Volcanol. Geotherm. Res.*, *88*, 99–107.

Zhao, W.-L., and W. J. Morgan (1985), Uplift of Tibetan plateau, *Tectonics*, *4*, 359–369.

Zhao, W.-L., and W. J. Morgan (1987), Injection of Indian crust into Tibetan lower crust: A two-dimensional finite element model study, *Tectonics*, *6*, 489–504.

Zhao, W., et al. (2001), Crustal structure of central Tibet as derived from project INDEPTH wide-angle seismic data, *Geophys. J. Int.*, *145*, 486–498.

M. Grove, T. M. Harrison, J. L. D. Kapp, and O. M. Lovera, Department of Earth and Space Sciences, University of California, Los Angeles, CA 90095, USA. (jkapp@southgateaz.org)

P. Kapp, Department of Geosciences, University of Arizona, Tucson, AZ 85721, USA.

D. Lin, Institute of Tibetan Plateau Research, Chinese Academy of Sciences, Beijing 100864, China.